Eur. Phys. J. C (2025) 85:673
https://doi.org/10.1140/epjc/s10052-025-14339-y

THE EUROPEAN PHYSICAL JOURNAL C

Regular Article - Theoretical Physics

The determination of potential scales in 2+1 flavor QCD

Tom M. B. Asmussen[a], **Roman Höllwieser**, **Francesco Knechtli**, **Tomasz Korzec**

Department of Physics, University of Wuppertal, Gaußstraße 20, 42119 Wuppertal, Germany

Received: 19 December 2024 / Accepted: 21 May 2025

Abstract We calculate the hadronic scales r_0, r_1 and their ratio r_0/r_1 on $N_f = 2 + 1$ flavor QCD ensembles generated by the CLS consortium. These scales are determined from a tree-level improved definition of the static force on the lattice, which we measure using Wilson loops. Our analysis involves various continuum and chiral extrapolations of data that cover pion masses between 134 MeV and 420 MeV and five lattice spacings down to 0.039 fm. We compare the potential scales to gradient flow scales by forming corresponding ratios. We find $r_0 = 0.4757(64)$ fm at the physical point. As a byproduct of our analysis we express the $N_f = 3$ QCD Lambda parameter determined by the ALPHA Collaboration in units of the scale r_0 and obtain $r_0 \Lambda^{(3)}_{\overline{\text{MS}}} = 0.820(28)$. Furthermore we present results for the second derivative of the potential to study its shape and compare it to phenomenological potential models.

1 Introduction

One of the essential requirements in lattice QCD calculations is the determination of the scale, i.e. of the lattice spacing in physical units. Among various scales used in lattice Quantum Chromodynamics (QCD), the r_0 scale [1] has been used in practical computations for a long time. The r_0 scale is convenient due to its simple definition in terms of the static quark anti-quark potential $V_0(r)$, which can be computed via Wilson loops [2]. On the other hand, the determination of r_0 from experimental input is not straightforward and is only indirect, since it involves phenomenological potential models.

Computations of Wilson loops established an understanding of confinement and its interplay with asymptotic freedom, a central problem of particle physics, via the formation of a flux tube between quark–anti-quark static charges [3–10]. Confinement manifests itself in the asymptotic linear rise of $V_0(r)$ at large r; the corresponding slope is known as the string tension. In quenched calculations, the scale has been set using the string tension, but in full QCD the string breaks at the pair-production threshold, making a precise definition difficult [11,12]. Instead of the string tension, one can consider the force $F(r) \equiv dV_0(r)/dr$ and form the dimensionless product $r^2F(r)$. The latter can be used to set the scale at distances defined by $r_i^2 F(r_i) = c_i$, with $c_0 = 1.65$ [1], $c_1 = 1$ [13], or $c_2 = \frac{1}{2}$ [14]. The definition of r_0 amounts to $r_0 \approx 0.5$ fm in phenomenological potential models.

In this work, we determine the r_0 and r_1 scales on the ensembles of gauge configurations generated by the Coordinated Lattice Simulations (CLS) initiative [15,16]. These ensembles include the dynamics of the three light (up, down and strange) quarks. The CLS consortium has produced these ensembles with an improved lattice action, high statistics, and multiple lattice spacings, making them particularly suitable for precision calculations. Incorporating the r_0 scale into the analysis of CLS ensembles offers valuable insights into the continuum and physical quark mass limits.

The article is organized as follows: First, we introduce the potential between a quark and anti-quark in the static limit and discuss its properties in Sect. 2. Then in Sect. 3 we describe the ensembles used in this work which were generated by the CLS consortium. Next, we present our determination of the scales r_0 and r_1 in Sect. 4. We perform various continuum and chiral extrapolations of the scales r_0 and r_1 in units of the gradient flow scale $\sqrt{t_0}$ [17] as well as the ratio r_0/r_1 in Sect. 5. We draw our conclusions by quoting our final results for the potential scales and the $N_f = 3$ QCD Λ parameter in units of r_0 in Sect. 6. There we also discuss the shape of the static potential at distances smaller than the string breaking distance and compare it to potential models.

[a] e-mail: t.m.b.a@gmx.de (corresponding author)

Published online: 19 June 2025

2 The static potential

The potential $V(r)$ between a static quark and anti-quark separated by a distance r from each other is one of the most fundamental and conceptually simplest quantities computable in QCD. At short distances it is very well described by perturbation theory and calculations to two and three loop order have been completed [18,19,19–22] both in pure gauge theory and in full QCD. Renormalized couplings can be defined both from the potential directly [23] (the V-scheme),

$$\alpha_V(\mu) = -\frac{1}{C_F} r V(r)\Big|_{\mu=r^{-1}}, \tag{2.1}$$

but also from the static force $F(r) \equiv V'(r)$ [1] or even from $V''(r)$ [24],

$$\alpha_{qq}(\mu) = \frac{1}{C_F} r^2 V'(r)\Big|_{\mu=r^{-1}}, \tag{2.2}$$

$$\alpha_c(\mu) = -\frac{1}{2C_F} r^3 V''(r)\Big|_{\mu=r^{-1}}. \tag{2.3}$$

The shape of the potential, or the force, at short distances is related to the β-functions of these couplings, which are known to 4 loops, derived from the 3-loop calculations of the potential together with the 4-loop β-function [25,26] of the $\overline{\text{MS}}$-coupling.

At long distances without dynamical fermions, the potential is expected to follow predictions from effective string theories [8,27]

$$V(r) = \sigma\, r + \mu + \frac{\gamma}{r} + O(1/r^2), \qquad \gamma = -\frac{\pi}{24}(d-2), \tag{2.4}$$

where σ is the string tension, μ is a regularization dependent mass and γ is a coefficient that depends on the space-time dimensionality d and which is universal across a wide range of effective string theories. Potential models [28] assume a certain shape of the static potential to predict heavy meson spectra. Over the years different phenomenological potentials have emerged, one being the Cornell potential [29]

$$V_{\text{Cornell}}(r) = -\frac{0.52}{r} + \frac{r}{(2.34\ \text{GeV}^{-1})^2}, \tag{2.5}$$

another the Richardson potential [30]

$$V_{\text{Richardson}}(r) = \frac{8\pi}{33-2N_f}\Lambda\left(\Lambda r - \frac{f(\Lambda r)}{\Lambda r}\right), \tag{2.6}$$

$$f(t) = \frac{4}{\pi}\int_0^\infty \mathrm{d}q\, \frac{\sin(qt)}{q}\left[\frac{1}{\ln(1+q^2)} - \frac{1}{q^2}\right], \tag{2.7}$$

where $N_f = 3$, $\Lambda = 398$ MeV was used in the original publication. In full QCD the string picture is only approximate, because the string "breaks" at a distance around $r \approx 1.2$ fm [11,12,31], and $V(r)$ smoothly transitions from being a static quark potential to being a (very flat) static-light molecule potential. At intermediate distances and in full QCD, the potential is best computed numerically in the framework of lattice QCD. When computed on a lattice with lattice spacing a, $V(r)$ contains a linearly divergent constant $E_{\text{self}}(a) \sim \frac{1}{a}$ [32,33], hence the static force, in which this is absent, is more widely used. An important application is the definition of hadronic scales [1,13]

$$r_1^2 F(r_1) = 1 \quad \text{or} \quad r_0^2 F(r_0) = 1.65. \tag{2.8}$$

They play an important role when lattice calculations are compared to each other and a dependence on experimental inputs is undesired. One example is the Λ parameter of QCD, which often is published in r_0-units [34]. In more recent times the r_0 scale is increasingly being replaced by gradient flow scales like t_0 [17] or w_0 [35] which are maybe more abstract, but easier to compute to a high precision. However the deep theoretical understanding and the mild lattice artifacts of r_0 make it still an appealing choice.

3 Simulations

For our calculation we use a subset of the gauge field ensembles generated by the CLS consortium [15,16]. These were generated using a Lüscher–Weisz-gauge action [36] with $N_f = 2+1$ flavors of dynamical $O(a)$ improved Wilson quarks [37,38]. The ensembles cover pion masses from the $SU(3)$-symmetric mass point with $m_\pi \approx 420$ MeV down to the physical pion mass, along trajectories where the sum of bare quark masses stays constant. Five different lattice spacings between 0.039 and 0.085 fm are available. The lattices have periodic boundary conditions for both gauge and fermion fields, except for the temporal direction which has either anti-periodic fermionic boundaries or, especially on all fine lattices, open boundaries [39]. In case of open boundaries, tree-level values for the fermionic and gluonic boundary improvement coefficients were used.

An even-odd preconditioned hybrid Monte-Carlo [40] with frequency splitting [41] of the quark determinant was used for the light quark doublet. The strange quark was treated with an RHMC [42]. For further details concerning the simulation algorithm we refer the reader to [43] and the documentation of the `openQCD` package [44].

The simulated gauge field distribution deviates slightly from the desired target distribution and all observables are corrected by the inclusion of a reweighting factor. This accounts for twisted-mass-reweighting [45,46], imperfections of the rational approximation and an occasionally negative strange quark determinant [47].

Keeping the sum of bare quark masses constant along a chiral trajectory is almost equivalent to keeping a suitable combination of pion and kaon masses constant. In nature the dimensionless combination $\phi_4 := 8t_0(m_K^2 + m_\pi^2/2)$ has a

Table 1 CLS ensembles used in this work. The ensembles are labeled by and id. For the H102 and N300 ensembles, runs with the same physical but different simulation parameters exist. The table furthermore lists the inverse bare coupling β, the lattice sizes, the boundary conditions in time direction (b.c.), where "o" stands for open and "p" for (anti-)periodic, the bare quark masses parametrized by the hopping parameters for up/down and strange quarks, the pion mass in MeV taken from [48] and the statistics in molecular dynamic units. The final entry is a rough estimate of the exponential autocorrelation time, which is used during error analysis to attach "tails" to auto-correlation functions

β	id	$\frac{T}{a} \times \frac{L^3}{a^3}$	b.c	$(\kappa_{u,d}, \kappa_s)$	m_π [MeV]	Stat. [MDU]	τ_{exp} [MDU]
3.40	H101	96×32^3	o	(0.13675962, 0.13675962)	420	8064	26.6
	H102-0	96×32^3	o	(0.136865, 0.136549339)	353	3988	26.6
	H102-1	96×32^3	o		356	4032	26.6
	H105	96×32^3	o	(0.13697, 0.13634079)	281	7880	26.6
	C101	96×48^3	o	(0.137055, 0.136172656)	221	8000	26.6
3.46	B450	64×32^3	p	(0.13689, 0.13689)	424	6448	32.9
	S400	128×32^3	o	(0.136984, 0.136702387)	357	11492	32.9
	D450	128×64^3	p	(0.137126, 0.136420428639937)	220	2000	32.9
	D452	128×64^3	p	(0.137163675, 0.136345904546)	157	3996	32.9
3.55	N202	128×48^3	o	(0.137, 0.137)	418	7608	47.3
	N203	128×48^3	o	(0.13708, 0.136840284)	350	6172	47.3
	N200	128×48^3	o	(0.13714, 0.13672086)	288	6848	47.3
	D200	128×64^3	o	(0.1372, 0.136601748)	200	8004	47.3
	E250	192×96^3	p	(0.137232867, 0.136536633)	131	3800	47.3
3.70	N300-0	128×48^3	o	(0.137, 0.137)	427	2028	77.9
	N300-1	128×48^3	o		427	5916	77.9
	J303	192×64^3	o	(0.137123, 0.1367546608)	260	8584	77.9
	E300	192×96^3	o	(0.137163, 0.1366751636177327)	177	4548	77.9
3.85	J500	192×64^3	o	(0.136852, 0.136852)	416	11552	126.5
	J501	192×64^3	o	(0.1369032,0.136749715)	339	14236	126.5

value very close to 1.098 [48]. All our ensembles deviate only slightly from this value. The physical mass point has $\phi_2 := 8t_0 m_\pi^2 = 0.0779(7)$ [48], which at the flavor symmetrical point should be $2\phi_4/3$. Slight mistunings of the masses are inevitable, and therefore our symmetric point ensembles do not all have exactly the same ϕ_2 values, and the chiral trajectories do not have exactly constant ϕ_4 values. In the past such mistunings were corrected by computing quark mass derivatives of all observables and using these to shift the results [49]. In this work the main focus is on purely gluonic observables and on dimensionless ratios of gluonic observables. In such cases the quark mass dependence is mild enough to simply ignore the mistunings. This has been observed in [49], where the necessary shifts in the gluonic quantity t_0 were insignificant, but it is also what we observe for potential scales on the ensembles where we computed the quark mass derivatives. For example on ensemble D450, ϕ_4 needs to be reduced by 0.51%. This changes r_0 by only 0.46 ‰, which is negligible, given that its statistical error is 0.45%. In the end, we avoid using the rather noisy quark mass derivatives, and instead take the mistuning into account by including terms proportional to $(\phi_4 - 1.098)$ in some of our fits.

The data analysis of auto-correlated Monte-Carlo time series is treated with the Γ-method [50]. An estimate of the exponential autocorrelation time τ_{exp} is used to take slowly decaying modes of the auto-correlation functions into accounts, as proposed in [51]. "Derived observables", i.e. non-linear functions of Monte-Carlo estimates, are conveniently treated as described e.g. in [52–54], i.e. by storing their mean values and "projected fluctuations" in suitable structures. This greatly simplifies linear error propagation with full control over all correlations and auto-correlations.

Table 1 summarizes the simulations used for this study.

4 Determination of r_0/a and r_1/a

The potential $V(r)$ between a static (infinitely massive) quark and anti-quark separated by distance r can be extracted from the expectation values of Wilson loops, which are traces of products of links along rectangular paths extending in Euclidean time and one spatial direction. In this article we consider only $r/a \times T/a$ on-axis Wilson loops, but off-axis (non-planar) Wilson loops can also be used. More precisely, we compute

$$W^{(l,k)}(x_0, r, T) = \frac{a^3}{2L^3} \sum_{\mu=1}^{3} \sum_{\mathbf{x}} \times \left(\frac{\langle \mathcal{W}^{(l)}(x, x + r\hat{\mu})\, \mathcal{W}^{(0)}(x + r\hat{\mu}, x + r\hat{\mu} + T\hat{0})\, \mathcal{W}^{(k)\dagger}(x + T\hat{0}, x + r\hat{\mu} + T\hat{0})\, \mathcal{W}^{(0)\dagger}(x, x + T\hat{0}) w \rangle}{\langle w \rangle} + T \to -T \right), \tag{4.1}$$

where $\mathcal{W}^{(l)}(x, y)$ denotes a smeared straight Wilson line from x to y. We follow the method of [24] for the measurement of the of Wilson loops and use the `wloop` package [55]. All gauge links have been HYP2 smeared using parameters $\alpha_1 = 1.0, \alpha_2 = 1.0, \alpha_3 = 0.5$ [32,56], which amounts to a particular modification of the Eichten–Hill static action [57]. In addition the links for the spatial lines in $\mathcal{W}^{(l)}$ have undergone l iterations of 3D HYP smearing with $\alpha_2 = 0.6, \alpha_3 = 0.3$, which allows us to construct a variational basis of creation/anihilation operators. After each iteration we project the gauge fields onto $SU(3)$ as described in [32] and always use Eq. (2.24) and four iterations of Eq. (2.25) of [32] for the projection. The numbers of smearing iterations are scaled with the lattice spacing and are tabulated in Table 3 of Appendix A.1. Finally w denotes the overall reweighting factor, as described in the previous section.

Assuming that x_0 and $x_0 + T$ are sufficiently far away from the temporal lattice boundaries, each of the measured correlation functions possesses a spectral decomposition

$$W^{(l,k)}(x_0, r, T) = \sum_{n=0}^{\infty} c_n^{(l,k)}(r) e^{-V_n(r)T}, \tag{4.2}$$

with complex coefficients $c_n^{l,k} = c_n^{k,l*}$. At short to intermediate separations r, the lowest lying energy level $V_0(r) \equiv V(r)$ is the static potential. The level above, $V_1(r)$, can be an excitation of the static potential, a static potential with hadrons that have vacuum quantum numbers (e.g. two pions) or a pair of static-light mesons. Its nature can change depending on the distance.

The correlation matrix is Hermitian, $W^{(l,k)} = W^{(k,l)*}$, but with finite statistics, this symmetry has to be enforced by symmetrization, before W is used in a GEVP procedure to extract the energy levels [58–62].

In the statistical average of standard Monte Carlo lattice simulations, the signal of Wilson loops is the result of strong cancellations between positive and negative contributions. This leads to an exponentially growing noise-to-signal ratio which prevents the calculation of the potential at large distances. In pure gauge theory an exponential suppression of the statistical noise of Wilson loops can be achieved by the multi-hit (or one-link) method [63] and much further by the multilevel algorithm [64]. These algorithms are not applicable in presence of dynamical fermions due to the non-locality of the effective gauge action when the logarithm of the fermion determinant is included. HYP smearing is known to reduce the noise problem both in pure gauge theory and in full QCD. In pure gauge theory it was demonstrated in [65] that the use of HYP smeared links leads to a determination of the static potential comparable in precision to the multi-hit method. In [24] it was shown that this procedure leads to a determination of the potential between quark and anti-quark sources that agrees with the continuum potential up to $\mathcal{O}(a^2)$ effects (after renormalization).

4.1 Effects of open temporal boundaries

The observables can be averaged in the lattice time direction, but to avoid effects of the open boundaries only Wilson loops sufficiently far away from the boundary are taken into account in the average. To evaluate which cut to use, several values of the number N_{cut} of timeslices cut from the temporal boundaries have been analysed. The left side of Fig. 1 shows how the result for a particular Wilson loop $W(x_0, r, T)$ depends on the temporal position x_0, and our preferred cut position is indicated. On the right one can see how the final result for r_0, whose determination will be explained in a later chapter, varies with the position of the cut. Surprisingly, the effect of including data that is clearly affected by boundary effects, does not lead to large systematic errors in the final result. Even the extreme case, where all data is included is comfortably compatible with our preferred value (in red), that is free of boundary contaminations. The procedure to obtain r_0 from Wilson loops involves a GEVP and a subsequent plateau average of an effective energy. In this process differently sized Wilson loops enter, and effects of the open boundaries may cancel to some extent. In some ensembles the dependence of the final result on the cut is stronger than in the ensemble J500 displayed here. The main observation here is that the error increases when more data is discarded, while the central value remains almost constant.

In the end we set $N_{\text{cut}} = 15$ for the coarsest lattice and scale this number with the lattice spacing up to $N_{\text{cut}} = 33$ on the finest lattices.

The time-averaged and symmetrized Wilson loops $\overline{W}^{(l,k)}(r, T)$ enter a generalized eigenvalue problem

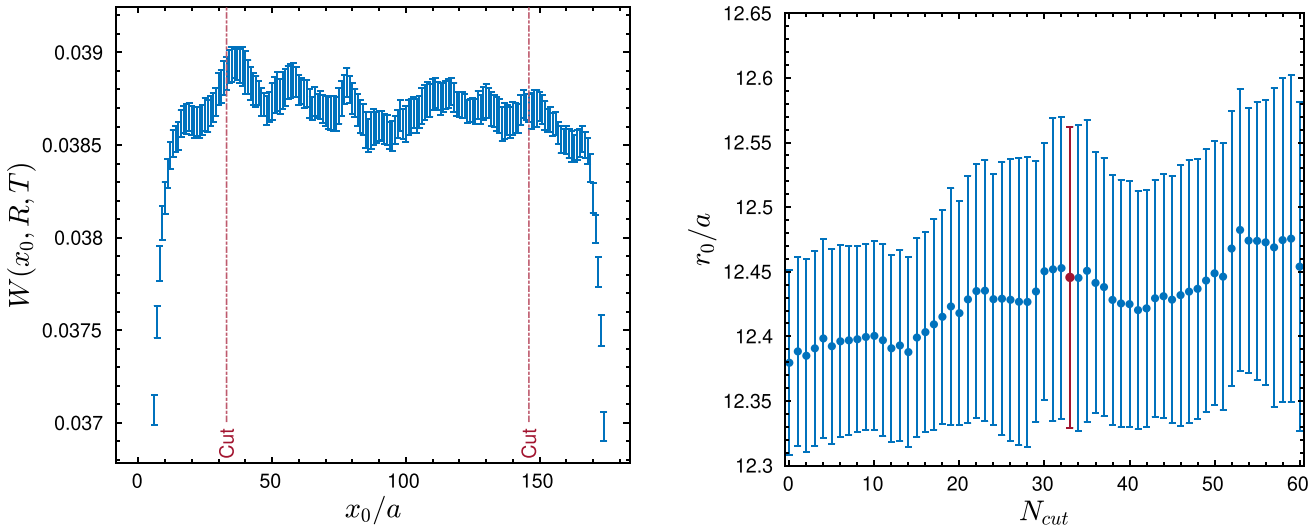

Fig. 1 On the left $W(x_0, r, T)$ as a function of x_0 is shown for ensemble J500 with loopsize $T = 13a$ and $r = 6a$ together with the cut of $N_{\text{cut}} = 33$ timeslices from the open boundaries in time. On the right we plot the dependence of r_0 on N_{cut}, with the red datapoint being a cut of 33

$$\overline{W}(r, T)\mathbf{v}_n = \lambda_n \overline{W}(r, T_0)\mathbf{v}_n, \tag{4.3}$$

with eigenvalues and eigenvectors that depend on T, T_0 and r. The n'th eigenvalue has the asymptotical form $\lambda_n(T, T_0, r) \propto e^{-V_n(r)(T-T_0)}$. The value for $T_0 = 5a$ is kept constant for all ensembles and distances r.

4.2 Improved distance for V, V', V''

Following [1] we eliminate tree level lattice artifacts by using the improved distance r_I

$$F(r_I) = [V(r) - V(r - a)]/a. \tag{4.4}$$

The tree level expression for the static potential extracted from Wilson loops using HYP smearing for the temporal lines has been derived in [66,67]. The improved distance r_I is defined such that the continuum tree level expression:

$$r_I^2 F_{\text{tree}}(r_I) = C_F \frac{g_0^2}{4\pi}, \tag{4.5}$$

where, for the gauge group SU(3) $C_F = 4/3$, holds exactly. On the lattice the tree level force is given by

$$F_{\text{tree}}(r_I) = -C_{\text{F}} \frac{g_0^2}{a} \int_{-\pi}^{\pi} \frac{d^3k}{(2\pi)^3} \times \frac{[\cos(rk_1/a) - \cos((r-a)k_1/a)] \times f_{\text{sm}}(k)}{4\left(\sum_{j=1}^{3} \sin^2(k_j/2) - 4c_1 \sum_{j=1}^{3} \sin^4(k_j/2)\right)}, \tag{4.6}$$

where the smearing factor f_{sm} is given in Eqs. (A.3) and (A.4) of [24]. With $c_1 = 0$ one would get the result for the plaquette action. In our case $c_1 = -1/12$ is used, which corresponds to the Lüscher–Weisz-gauge action. Similarly for the shape parameter $c(r)$ an improved definition can be found

$$c(\tilde{r}) = \frac{1}{2}\tilde{r}^3[V(r + a) + V(r - a) - 2V(r)]/a^2, \tag{4.7}$$

where $\tilde{r}$ is chosen such that

$$c_{\text{tree}}(\tilde{r}) = -C_F \frac{g_0^2}{4\pi}. \tag{4.8}$$

The values of the improved distances for the force $F(r_I)$ and for $c(\tilde{r})$ for our choice of HYP2 smearing can be found in Table 4 of Appendix A.2.

4.3 Evaluation of $V(r)$ and $F(r)$

The ground state potential $V(r)$ can be found by performing a weighted average in a plateau region of the effective masses $E_0(T, T_0, r) = \frac{1}{a}\ln(\lambda_0(T, T_0, r)/\lambda_0(T + a, T_0, r)$ extracted from the GEVP. Examples of effective masses are shown in Fig. 2. From top to bottom, the first row of plots show the dependence on the lattice spacing a, the second row the dependence on the pion mass m_π and the third row the dependence on the distance r.

On some ensembles it has been difficult to determine the crucial starting point of the plateau, especially for potentials around $r \approx r_1$. Therefore in contrast to previous work with these ensembles [68] we performed a fit to the effective masses of the form

$$E_0(T, T_0, r) = E_0 + Be^{-\Delta \cdot T}. \tag{4.9}$$

Where plateau averages were unproblematic, such fits yielded compatible values, but they have the advantage to be able to fit data at earlier times, in practice all data starting at T_0. A

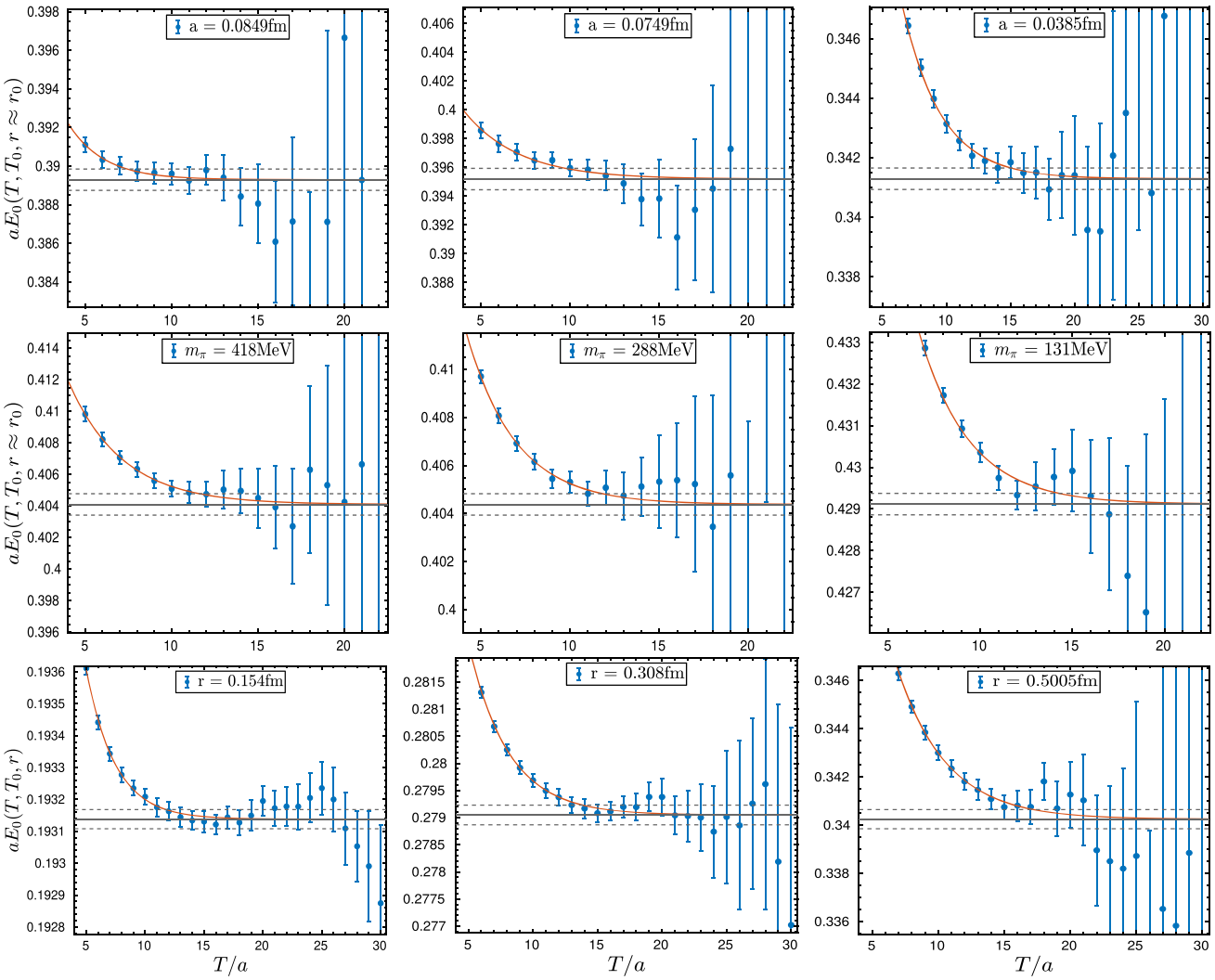

Fig. 2 Several effective mass plots. The first row shows the symmetric mass ensembles H101, B450, and J500 with decreasing lattice spacing at $r \approx r_0$. In the second row we display ensembles N202, N200, and E250 with decreasing pion mass from the symmetrical to physical value at $r \approx r_0$. The last row shows the finest lattice J501 at $m_\pi \approx 340$ MeV with different values of r from $\frac{r_1}{2}$ up to r_0

precise value of E_0 can be obtained even for cases where the traditional plateau starts very late or is non existent.

Unfortunately this nonlinear three parameter fit by itself was not stable enough for all effective masses on all ensembles to confidently describe the data and find the ground state everywhere. To fix this we invoked a two step process. First, the ensembles where this fit is unproblematic are used to extract the Δ parameter as a function of r, m_π and the lattice spacing. One global fit per lattice spacing is performed to establish a model for the Δ values. The ansatz for the global fit assumes that the "effective" excited state with energy $E_0+\Delta$ has an approximately constant energy as a function of r, and therefore the difference to $V(r)$ behaves like $V(r)$ itself,

$$\sqrt{t_0}\Delta = \hat{\Delta}_0 - \hat{\delta}_0 \frac{r}{\sqrt{t_0}} - \hat{\gamma}_0 \frac{\sqrt{t_0}}{r} + \hat{b}_0 t_0 \left(m_\pi^2 - \left(m_\pi^{\text{phys}} \right)^2 \right). \tag{4.10}$$

Once the four parameters $\hat{\Delta}_0$, $\hat{\delta}_0$, $\hat{\gamma}_0$, and $\hat{b}_0$ of this model are determined, it can be used to read off Δ on all ensembles, including those where fit Eq. (4.9) was unstable. That value is then used in fit Eq. (4.9), turning it into a well behaved linear fit with two parameters. In Fig. 3 one can see how well the model (Eq. (4.10)) describes the Δ values for $\beta = 3.55$. The first datapoints, which have large lattice artifacts, have not been used in the fit Eq. (4.10), but have been included visually in the figure. In the interesting range $r_1 \leq r \leq r_0$ the fit describes the data very well.

A fit of the effective mass using the gap from the global fit Eq. (4.10) can be seen on the left of Fig. 4, where the red line shows the fit and the darkgrey line the resulting ground state with the associated uncertainty as dashed lines.

Computing $F(r)$ from the potential $V(r)$ using the improved distance, see Eq. (4.4) one can find the values of r_1

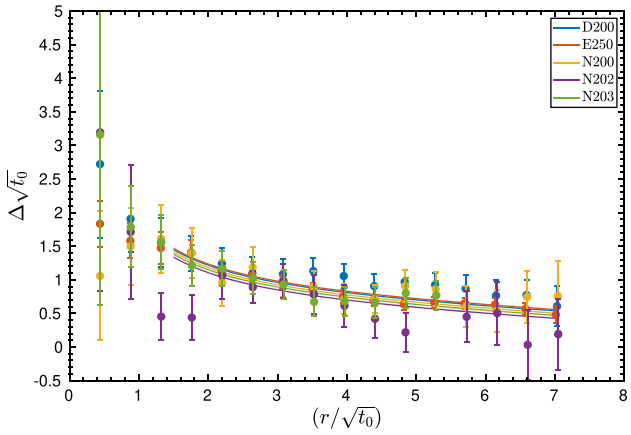

Fig. 3 Global fit of the gap Δ extracted from fits given in Eq. 4.9 for $\beta = 3.55$

and r_0 by Eq. (2.8) which is visualised in the right plot Fig. 4. Different interpolation ranges can be used to determine the values of r_1 and r_0. On the one hand a 2-point interpolation is used with the two points enclosing the target value. For a 3-point interpolation a third point is included, either corresponding to a smaller or to a larger distance than the points used in the 2-point interpolation. The interpolation function used for the 2- or 3-point interpolation is

$$F(r_I)r_I^2 = \hat{f}_1 r_I^2 + \hat{f}_0, \quad \text{(2-point)} \quad \text{or} \tag{4.11}$$

$$F(r_I)r_I^2 = \hat{f}_1 r_I^2 + \hat{f}_0 + \hat{f}_2/r_I^2, \quad \text{(3-point)}, \tag{4.12}$$

where $\hat{f}_0$, $\hat{f}_1$, and $\hat{f}_2$ are the coefficients of the interpolations. In Fig. 5 the three interpolations are shown by the lines with different colors. The purple line, which has an errorband, is the interpolation used for the final result. It uses three points with two points at smaller distances and one point at larger distance than the targeted value of r. One can see that the difference between the different interpolations is minuscule and the results are compatible with each other. For coarser lattice spacings lattice artifact might be enhanced when very small Wilson loops are used in the interpolation. The differences of the interpolations in r_1 is larger, as the forces have smaller errors, and the $1/r^2$ terms are larger in this region.

4.4 Evaluation of exceptionally problematic ensembles

For a very small number of ensembles and distances, the determination of the potential from effective energies has been particularly difficult. In particular, we observed problems where r was close to r_1 on ensembles with finer lattice spacings. A plot of one of the most problematic cases, the effective mass of ensemble E300, is shown in Fig. 6. E300 has the second finest lattice spacing with a pion mass close to the physical one. A dip of the effective mass can be observed here at large T/a. Several methods have been used to analyze and possibly find a better way to determine the potential for this case. We mostly focussed on E300, as the pion mass was close to the physical mass. At first we doubled the amount of different smearing levels. The hope was to be able to better suppress excited states, with a larger basis for the GEVP. Unfortunately this did not bring the desired improvement of the effective energy.

Then we looked at different more complicated fit functions for the effective masses, for example by adding an additional excited state contribution to Eq. (4.9) that is either fixed to be two pion masses above E_0 or left free. Adding this second exponential term proved to make the fit less stable for a lot

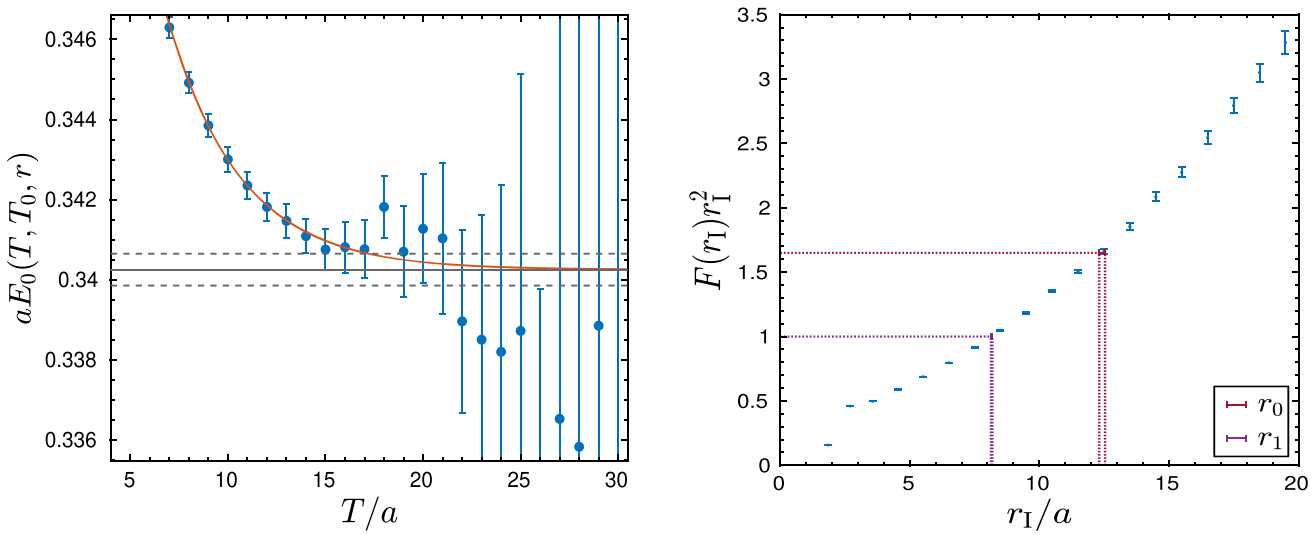

Fig. 4 The effective masses for ensemble J500 at $r/a = 13$ with $t_0/a = 5$ on the left together with the fit Eq. 4.9 in red and the ground state potential as the grey line. On the right is the static force $F(r)$ of the same ensemble together with the values r_0 and r_1 of the 3-point interpolation

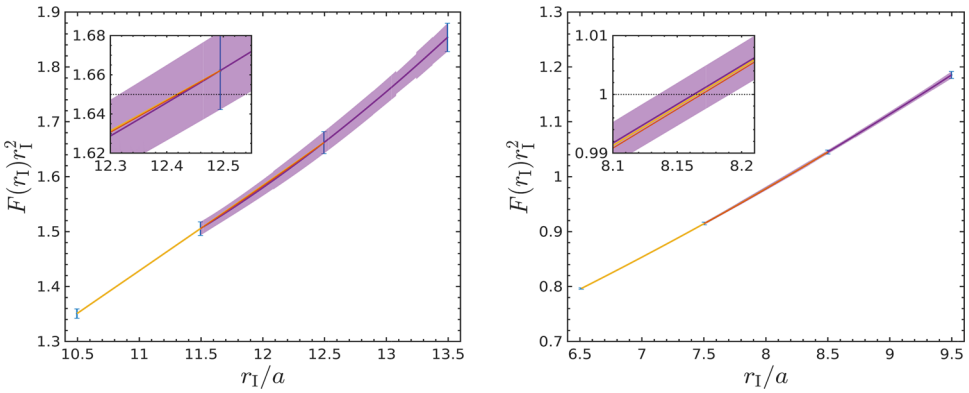

Fig. 5 We show the three different interpolations for r_0 (left) and r_1 (right). The red line corresponds to the 2-point interpolation using the nearest points to the target r-value. The yellow line uses the same points and one point at a shorter distance. The purple line is with one point at a larger distance. The purple line is the one used for the final result and has an included errorband. On the top left of the figure is a zoomed in view of the point of interest

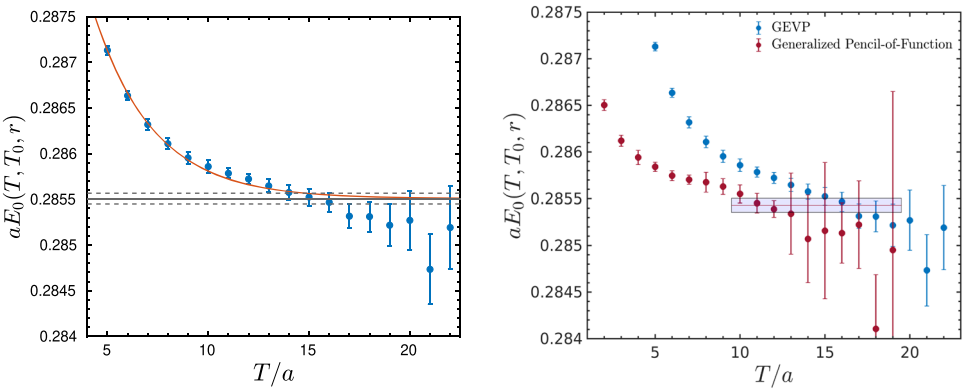

Fig. 6 On the left ensemble E300 with a loopsize of $r/a = 6$, which is in the range of r_1, showing the plateau calculation using the fit method described in Sect. 4.3. The right figure shows the difference between using the GEVP method in blue and the effective mass calculated through the pencil of function method in red for E300

of ensembles, so that the fit form in Eq. (4.10), did not work any more.

The method used in the end for this difficult case is the pencil of functions method [62,69–72], which seems to produce a more reliable plateau albeit with a larger error. The method expands the original 4×4 correlation matrix to an 8×8 in which every element $\overline{W}^{(k,l)}(r, T)$ of the original matrix is replaced by $\begin{pmatrix} \overline{W}^{(k,l)}(r, T) & \overline{W}^{(k,l)}(r, T+\tau) \\ \overline{W}^{(k,l)}(r, T+\tau) & \overline{W}^{(k,l)}(r, T+2\tau) \end{pmatrix}$. We use $\tau = 2a$ here. This larger matrix is "pruned" [73] down to 6×6, before the GEVP problem is solved as before. A difference between the "normal" effective energies and the ones calculated with this new method can be seen on the right of Fig. 6 for the E300 ensemble.

Other cases in which the plateau was not well defined were ensembles B450 and J501. In the latter only in the range of r_1. The problems seem to be unrelated to the quark mass or resolution of the lattices, as it did not appear for E250 at the physical pion mass nor for other ensembles at the fine lattice spacing.

5 Continuum and chiral extrapolations

Using the methods explained in the previous chapter a value for r_0/a and r_1/a is determined and collected in Table 5 of Appendix A.3 for each of the 18 ensembles. A plot with the values together with a global fit of the form

$$\frac{r_0}{a} = c_1|_\beta + c_2(r_0 m_\pi)^2 \tag{5.1}$$

is shown in Fig. 7. For both r_0 and r_1 the pion mass dependence is very mild, leading to nearly horizontal trends of the fit functions. Note that the data point for E300 (purple point farthest to the left) is more than one sigma away from the fit which we also observe for r_0/r_1 and $r_1/\sqrt{t_0}$. The results of the scales extrapolated to the physical value of m_π and to chiral limit ($m_\pi = 0$) can be found in Table 2. These results will be used in Sect. 6.2 to calculate $\Lambda \times r_0$.

For the next step we combine our values of r_0 and r_1 with $\sqrt{t_0}$ into a dimensionless ratio. Statistical correlations between the quantities entering the ratios are propagated into our analysis. Such ratios are independent of the overall scale and data from different lattice spacings fall onto a universal curve (a function of m_π), up to lattice artifacts. A combined continuum and chiral (inter[1]-)extrapolation requires an ansatz that models the lattice artifacts and the mass dependence. The global fit used in Fig. 8 is of the form

$$\text{Fit 1}: \quad \frac{r_0}{\sqrt{t_0}} = c_1^{(1)} + c_2^{(1)} \left(\frac{a}{r_0^{\text{sym}}}\right)^2 + c_3^{(1)}(r_0 m_\pi)^2, \tag{5.2}$$

[1] One ensemble is generated at the physical pion mass.

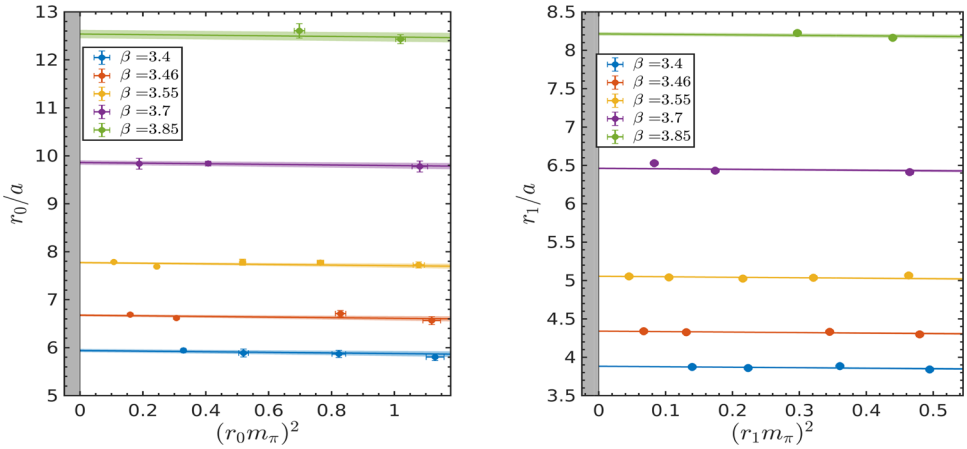

Fig. 7 r_0/a and r_1/a for all ensembles as a function of $(r_0 m_\pi)^2$ (left) and $(r_1 m_\pi)^2$ (right). A global fit Eq. (5.1) is performed on the data

where r_0^{sym} is the value for the ensembles calculated at the symmetric point with degenerate quark masses. This particular fit assumes that lattice artifacts are purely $O(a^2)$ and do not depend on the mass. The physical mass dependence is assumed to be linear in m_π^2. The symmetric ensembles correspond to the point farthest to the right for each lattice spacing. Ideally these points would be on top of each other, but scatter slightly because of the mistunings, as discussed in Sect. 3. The black/grey band on the bottom of the figure shows the mass dependence in the continuum limit by setting c_2 in Eq. (5.2) to zero. Using the physical mass of the pion $m_\pi = 134.8$ MeV (after correcting for isospin breaking effects [49]) and the physical value of $\sqrt{t_0} = 0.1443(7)(13)$ fm [48] the physical value for r_0 can be extrapolated.

In addition to looking at all data, in Fig. 8, we plot the data at the symmetric mass point as a function of a^2 to visualize the continuum extrapolation entailed in the fit. The solid lines in Fig. 9 are the fit functions evaluated setting $(r_0 m_\pi)^2 = 1.1$ and $(r_1 m_\pi)^2 = 0.47$ in Eq. (5.2) respectively. The fit curve follows the displayed data nicely, even if it comes from a global fit including all data.

Complementing the fit defined in Eq. (5.2), which is labeled as F_1, three other fits are performed on the $r_0/\sqrt{t_0}$ data with changed or added terms,

$$\text{Fit 2}: \quad \frac{r_0}{\sqrt{t_0}} = c_1^{(2)} + c_2^{(2)} \left(\frac{a}{r_0^{\text{sym}}}\right)^2 + c_3^{(2)} (r_0 m_\pi)^2 + c_4^{(2)} (m_\pi a)^2, \tag{5.3}$$

$$\text{Fit 3}: \quad \frac{r_0}{\sqrt{t_0}} = c_1^{(3)} + c_2^{(3)} \left(\frac{a}{r_0^{\text{sym}}}\right)^2 + c_3^{(3)} \phi_2 + c_4^{(3)} (1.098 - \phi_4), \tag{5.4}$$

$$\text{Fit 4}: \quad \frac{r_0}{\sqrt{t_0}} = c_1^{(4)} + c_2^{(4)} \left(\frac{a}{t_0^{\text{sym}}}\right)^2 + c_3^{(4)} \phi_2 + c_4^{(4)} (1.098 - \phi_4). \tag{5.5}$$

Table 2 Results of $\frac{r_0}{a}$, $\frac{r_1}{a}$ in the chiral limit ($m_\pi = 0$, superscript "χ") and at the physical point (no superscript)

β	r_0^χ/a	r_0/a	r_1^χ/a	r_1/a
3.4	5.941(35)	5.934(35)	3.883(8)	3.880(8)
3.46	6.676(26)	6.670(26)	4.341(6)	4.338(6)
3.55	7.773(21)	7.766(21)	5.055(5)	5.052(5)
3.7	9.860(46)	9.854(46)	6.462(12)	6.460(12)
3.85	12.540(88)	12.533(88)	8.214(23)	8.211(23)

The second fit labeled F_2 defined in Eq. (5.3) is similar to Fit 1, but with an added term that parameterizes mass dependent lattice artifacts. In Fits 3 Eq. (5.4) and 4 Eq. (5.5) we allow for a mistuning of data with respect to the desired value $\phi_4 = 1.098$. In Fit 3 the lattice artifact is $\propto a^2/r_0^{\text{sym}}$, while Fit 4 uses a^2/t_0^{sym}.

To further investigate possible systematic errors, several cuts on the data are performed. Either one or two of the coarsest lattices are neglected. In addition data too far away from the physical mass point can be excluded. The mass cut, when in place, eliminates all data at the symmetrical mass point. Results of r_0 depending on the different fits and cuts together with their associated $\chi^2/d.o.f.$ can be found in Table 6 in Appendix A.4 and visualized in a plot in Fig. 10. All in all the extrapolated values are in agreement with each other. The main effect of the cuts is a slight increase in error. The biggest disparity is observed for r_1 when discarding the coarsest 2 lattice spacings. An explanation might be that with the cuts in place the slightly out-lying E300 value gets a relatively higher statistical weight. In the initial phase of the analysis we considered computing the derivative of all observables with respect to ϕ_4 and applying a mistuning correction on all ensembles, but since Fit 3 and Fit 4 yield very similar results to the fits without a parameterization of the mistunings, we did not deem the correction to be necessary. Especially since these derivatives are quite noisy for purely gluonic observables. The final values are given by an average according to

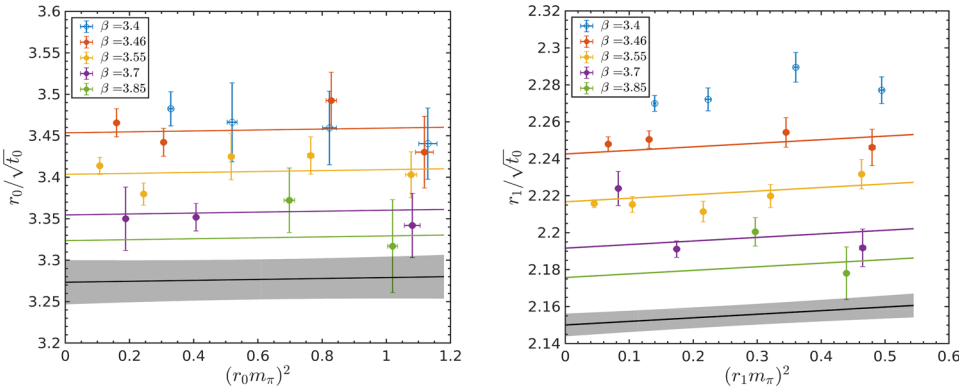

Fig. 8 On the left the values $r_0/\sqrt{t_0}$ and the right $r_0/\sqrt{t_0}$ are plotted together with a global fit corresponding to Fit 1 in Eq. 5.2. The grey band on the bottom corresponds to the continuum extrapolation of said fit

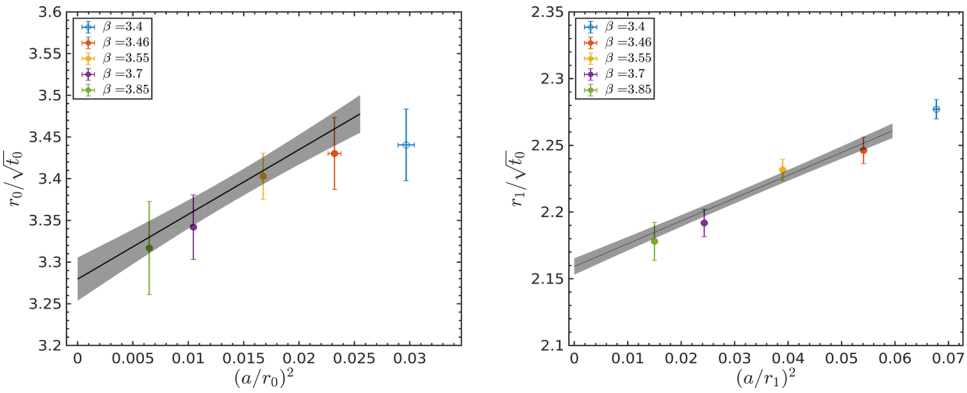

Fig. 9 The same fits as in Fig. 8 displayed as a function of the lattice spacing at the symmetric point

the Akaike Information Criterion [74–77], short AIC.

$$\langle \mathcal{O} \rangle = \sum_{n=1}^{N_{\text{fits}}} w_n^{\text{AIC}} \langle O \rangle_n, \tag{5.6}$$

where the AIC weight for a given fit and cut labelled by n is given by

$$w_n^{\text{AIC}} = N \exp\left[-\frac{1}{2} (\chi_n^2 + 2N_n^{\text{parameters}} + 2N_n^{\text{cut}} \right]. \tag{5.7}$$

N is a normalization factor, $N_n^{\text{parameters}}$ the number of fit parameters for a given fit, and N_n^{cut} the number of excluded datapoints. The points with the coarsest lattice spacing are excluded in the overall average, which is visualized by the empty markers in the figure.

The same analysis is repeated for the values of r_0/r_1, seen on the left of Fig. 11, where the fit corresponding to the grey band in the plot is done using a linear fit similar to Eq. (5.2). On the right of the same figure the different fits and cuts are seen together with the AIC average. Compared to $r_0/\sqrt{t_0}$ and $r_1/\sqrt{t_0}$, the effect of the cuts is larger for r_0/r_1.

5.1 Corrections to leading scaling violations

Our continuum extrapolations assume pure $O(a^2)$ lattice artifacts. Symanzik's effective theory [78] for our action predicts subleading $O(a^3)$ artifacts, which we neglect. What is potentially more problematic, is that already the leading scaling violations are not expected to be of pure $O(a^2)$ form, but rather receive logarithmic corrections $O\left(a^2 \ln(a\Lambda)^{-\hat{\Gamma}}\right)$ [79–81]. The possible exponents $\hat{\Gamma}$ are related to anomalous dimensions of the various dimension 6 operators that enter the Symanzik action. They are known in perturbation theory and for our action have values like $\hat{\Gamma} \in \{-0.11111, 0.24731, 0.51852, \ldots\}$. More logarithmic corrections are expected that depend on the specific observables. Even if all possible exponents were known, performing a fit containing all such lattice artifact terms is simply impossible. To judge the potential impact of these logarithms we re-visit Fit 1, but instead of the pure $(a/r_0^{\text{sym}})^2$ term consider $(a/r_0^{\text{sym}})^2 \ln\left[r_0^{\text{sym}}/a\right]^{\hat{\Gamma}}$, in which we vary the $\hat{\Gamma}$ within a reasonable range. Figure 12 summarizes our findings. For the r_0 case we also show a few of the modified fits in Fig. 13. We conclude, that our procedure of investigating various different cuts on the data-set, e.g. neglecting the coarsest ($\beta > 3.4$), or the two coarsests ($\beta > 3.46$) lattice spacings leads to similar or greater spreads of the continuum val-

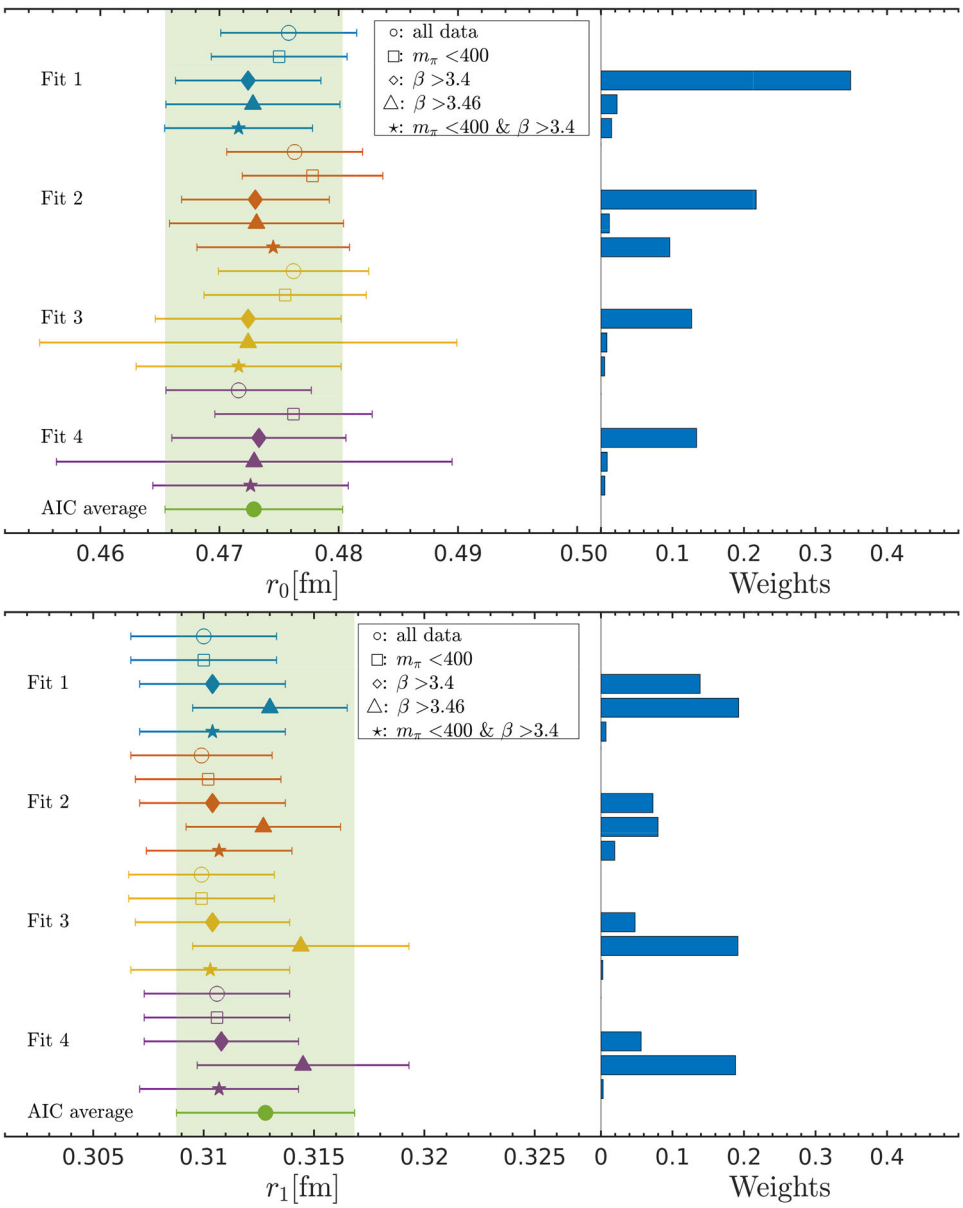

Fig. 10 The top panel shows the values of r_0 at the physical point obtained from the different fits listed in Table 6 of Appendix A.4 together with different cuts, as well as the weights (5.7). At the bottom the same is shown for r_1. The green point corresponds to the AIC average excluding the coarsest lattice spacing shown as empty markers

ues than allowing different logarithmic factors. For our final extrapolations we thus stay with $\hat{\Gamma} = 0$.

6 Results and conclusions

6.1 The scales r_0 and r_1

The main result of this work are the values of the scales r_0 and r_1 from the static force, as well as their ratio, at the physical mass point of $N_f = 2 + 1$ QCD,

$$r_0 = 0.4729(57)(48)\,\text{fm}, \tag{6.1}$$

$$r_1 = 0.3127(24)(32)\,\text{fm}, \tag{6.2}$$

$$\text{and} \quad \frac{r_0}{r_1} = 1.532(12). \tag{6.3}$$

In r_0 and r_1 the first error is from the uncertainty of the dimensionless ratio $r_i/\sqrt{t_0}$ in the continuum limit, as listed below, and the second error due to the scale $\sqrt{t_0}$ in fm [48]. Both should be combined in quadrature. For the dimensionless ratios $r_i/\sqrt{t_0}$ we obtain

$$\frac{r_0}{\sqrt{t_0}} = 3.277(39), \tag{6.4}$$

$$\text{and} \quad \frac{r_1}{\sqrt{t_0}} = 2.167(16). \tag{6.5}$$

Figure 14 compares these values with previous determinations for $N_f = 2 + 1$ together with the Flag average [34] and $N_f = 2 + 1 + 1$. In [97,98] it was shown that effects

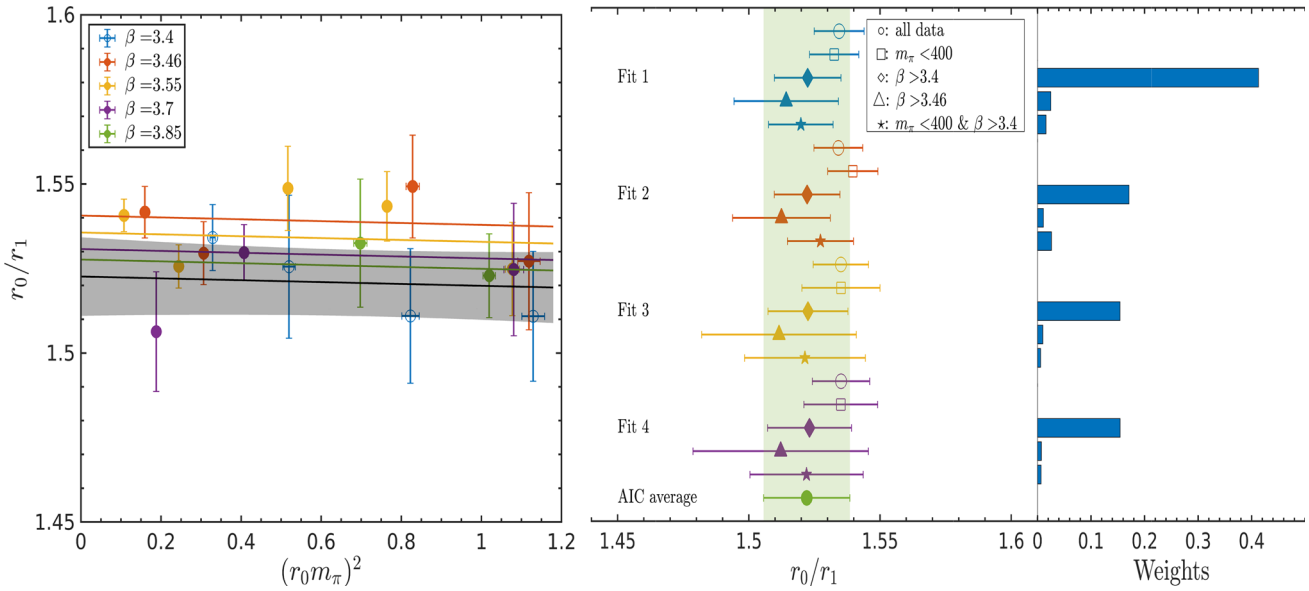

Fig. 11 On the left: the values of r_0/r_1 of the different ensembles together with a fit like Eq. (5.2). The grey band is the fit result in the continuum limit. On the right: the results of the different fits and cuts performed on the data together with the AIC average excluding the coarsest lattice spacing

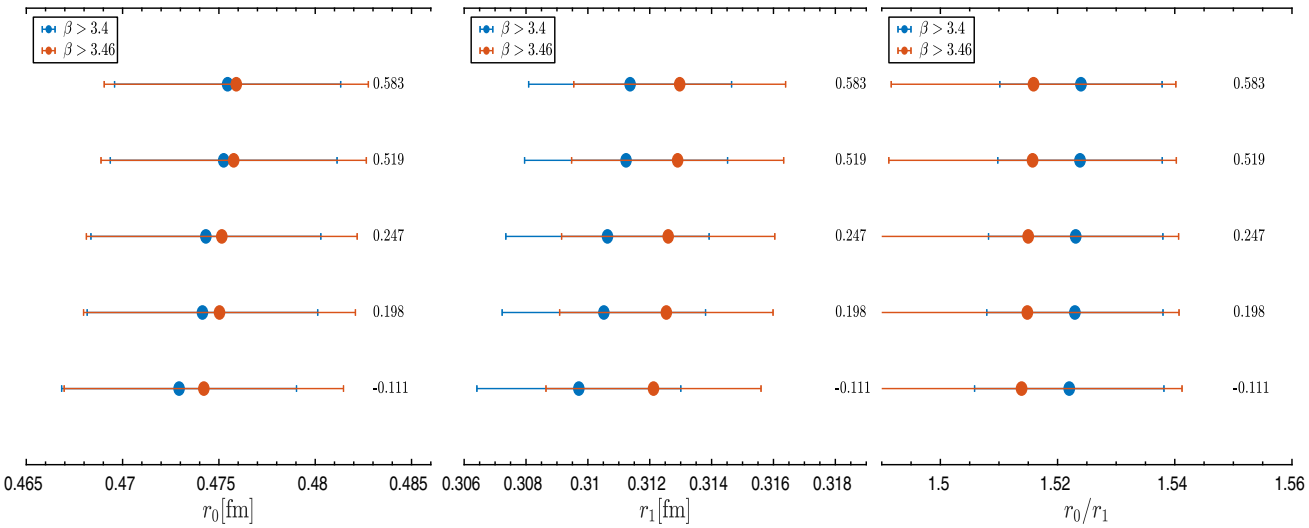

Fig. 12 The impact of logarithmic corrections on the continuum values of r_0 (left), r_1 (middle), and r_0/r_1 (right). Different colors refer to data sets with different cuts on the coarsest lattice spacing. The $\hat{\Gamma}$ used in the fit is printed to the right of the corresponding error bars

of a dynamical charm quark on ratios of low energy scales are typically at permille level. Thus we expect the results for the scales r_0, r_1 and the ratio r_0/r_1 to agree between $N_f = 2 + 1$ QCD and $N_f = 2 + 1 + 1$ QCD at the current level of accuracy. As a follow up to Sect. 4.4 an analysis has been performed where E300 has been removed from the calculations altogether. The result is that only the value of r_1 changes slightly within the errors. The values with the E300-cut in place are $r_0 = 0.4728(76)$ fm, $r_1 = 0.3106(37)$ fm, and $\frac{r_0}{r_1} = 1.526(17)$.

6.2 The Λ-parameter in units of r_0 for $N_f = 3$ QCD

The strong coupling "constant" is a fundamental parameter of QCD and a precise knowledge of its value of great importance for many predictions that QCD makes. The value of the coupling at any scale can be computed from its RG-equation, provided that the dimensionful Λ-parameter in that scheme is known. It has been a great success of lattice QCD to be able to produce the most accurate results for $\Lambda_{\overline{\text{MS}}}$ using only very precise low energy experiments as inputs (e.g. the masses and decay rates of pseudo-scalar mesons) [99]. To remove the additional complications of scale-setting from the results,

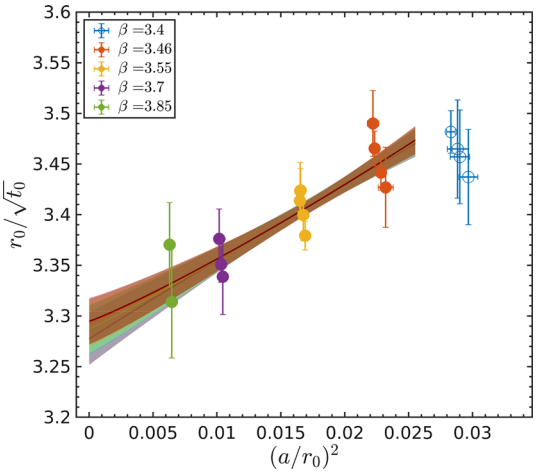

Fig. 13 Fits with different $(a/r_0^{\rm sym})^2$ $\ln\left[r_0^{\rm sym}/a\right]^{\hat{\Gamma}}$ terms. To plot all data together, the mass dependent part of the fit function was subtracted from the data, i.e. the displayed data is in the chiral limit. The bands correspond to the same $\hat{\Gamma}$ values as in Fig. 12, where the bottom one has $\hat{\Gamma} = -0.111$ and the top one 0.583

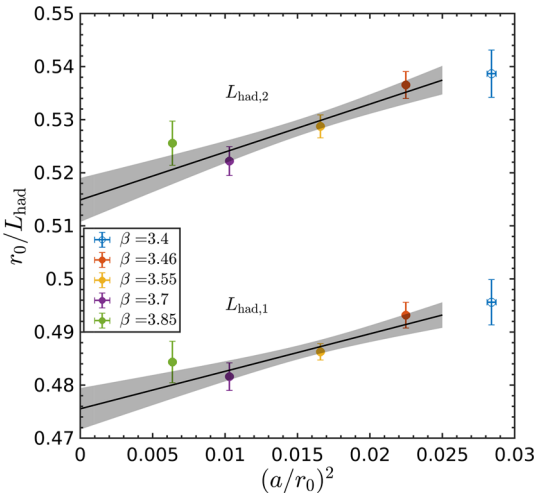

Fig. 15 Continuum extrapolations of the ratio of r_0/a over $L_{\rm had}/a$ for two definitions of the scale $L_{\rm had}$ as explained in the text

lattice collaborations often publish dimensionless intermediate results, that can be compared without setting the scale. These are typically the Λ-parameter in units of r_0, $\sqrt{t_0}$ or w_0. Values for $r_0\Lambda$ and $\sqrt{t_0}\Lambda$ are collected, assessed and averaged by the FLAG group [34] in addition to the results in MeV.

In recent years the r_0 units were largely replaced by scales based on the gradient flow, and e.g. the recent result of the ALPHA collaboration [100] has only used the latter. That particular calculation constructs the fully non-perturbative scale evolution of a coupling over a wide range of scales using a finite-size-scaling method. This procedure yields a value for $L_{\rm had}\Lambda^{(3)}_{\overline{\rm MS}}$ in the continuum limit of massless three flavor QCD, where $L_{\rm had}$ is some constant linear box size. In a last step $L_{\rm had}$ is traded for $\sqrt{t_0}$ by extrapolating the ratio of $L_{\rm had}/a$ over $\sqrt{t_0}/a$ to the continuum limit. For this to be possible, both quantities need to be known using the same lattice action at the same set of improved bare couplings $\tilde{g}_0^2$.

This was all carried out in [100], using two different definitions of $L_{\rm had}$, both implicitly defined by the gradient-flow coupling $\overline{g}_{\rm GF}(L_{\rm had}^{-1})$ having a particular value, namely

$$\overline{g}^2_{\rm GF}(L^{-1}_{\rm had,1}) = 11.31 \quad \to L_{\rm had,1}\Lambda^{(3)}_{\overline{\rm MS}} = 1.729(57), \tag{6.6}$$

$$\overline{g}^2_{\rm GF}(L^{-1}_{\rm had,2}) = 10.20 \quad \to L_{\rm had,2}\Lambda^{(3)}_{\overline{\rm MS}} = 1.593(53). \tag{6.7}$$

The finite lattice spacing results for $L_{{\rm had},i}/a$ were tabulated in Table V of the supplementary material of [100].

To obtain the Λ parameter in r_0 units, we could go ahead and multiply the original result for $\sqrt{t_0}\Lambda$ by our ratio $r_0/\sqrt{t_0}$. This would however involve two continuum extrapolations, namely the one for $L_{\rm had}/\sqrt{t_0}$ and ours from Sect. 5. But because we use the exact same action at the same set of improved bare couplings, we are in the fortunate position to be able to completely eliminate the flow quantity t_0 from the calculation and directly continuum extrapolate the ratio r_0/a

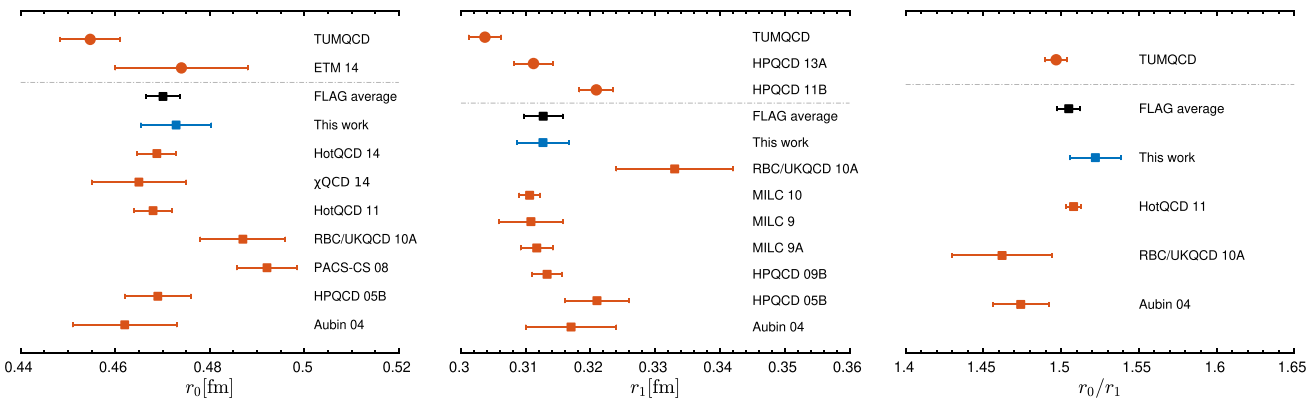

Fig. 14 Results of r_0 on the left, r_1 in the middle, and $\frac{r_0}{r_1}$ to the right. All of them are in comparison with the results from the FLAG review 2021. The upmost points represented by circles are calculated using $N_{\rm f} = 2+1+1$ QCD while the others are $N_{\rm f} = 2+1$ QCD [34,82–96]

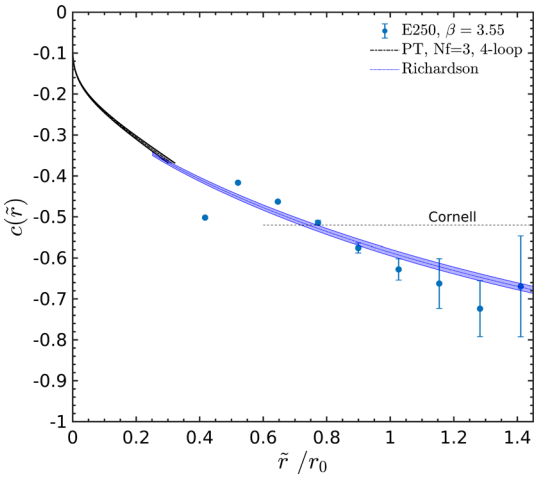

Fig. 16 The shape parameter $c(r)$ (Eq. (6.11) and its lattice definition Eq. (4.7)) for the ensemble E250 at the physical point is plotted as a function of the improved distance $\tilde{r}$ (defined through Eq. (4.8)) in units of r_0. For comparison we show the perturbative (PT) curve at short distance, the value $c = -0.52$ in the Cornell model Eq. (2.5) and the curve derived from the Richardson potential Eq. (2.6)

over $L_{\rm had}/a$. This extrapolation turns out to be very well behaved and is shown in Fig. 15, yielding

$$\frac{r_0}{L_{\rm had,1}} = 0.4755(39) \quad \to r_0\Lambda^{(3)}_{\overline{\rm MS}} = 0.822(28), \tag{6.8}$$

$$\frac{r_0}{L_{\rm had,2}} = 0.5149(41) \quad \to r_0\Lambda^{(3)}_{\overline{\rm MS}} = 0.820(28), \tag{6.9}$$

both in good agreement with the FLAG average $r_0\Lambda^{(3)}_{\overline{\rm MS}} = 0.808(29)$, which includes the calculations [100–106]. Both values of the Λ parameter in r_0 units, Eqs. (6.8) and (6.9) are equally good and we quote

$$r_0\Lambda^{(3)}_{\overline{\rm MS}} = 0.820(28) \tag{6.10}$$

as our final result.

6.3 Shape of the potential

The renormalized quantity

$$c(r) = \frac{1}{2}r^3V''(r) \tag{6.11}$$

can be used to study the shape of the static potential. At short distances $r \to 0$ the dependence of $c(r)$ on the distance r is governed by the renormalization group equation. This is because of the relation to the renormalized coupling $\alpha_c(\mu) = -c(r)/C_{\rm F}$ given in Eq. (2.3). At large distance the behaviour of $c(r)$ depends on the flavour content. In pure gauge theory it approaches asymptotically the value $c(\infty) = \gamma = -\pi(d-2)/24$, see Eq. (2.4). In a theory with dynamical fermions string breaking happens and so $c(\infty) = 0$ due to the flattening of the ground state static potential. Therefore we expect $c(r)$ to be very sensitive to sea quarks effects.

For these reasons $c(r)$ is an interesting quantity to be studied by lattice simulations. An improved lattice definition of $c(r)$ is given in Eq. (4.7), in terms of a distance $r = \tilde{r}$ chosen such that at tree level in perturbation theory $\alpha_{c,\rm tree} = g_0^2/(4\pi)$, cf. Eq. (4.8). Precise values of $c(r)$ have been calculated in pure gauge theory in [8] using a multi-level sampling algorithm. They have been compared to lattice results from $N_{\rm f} = 2$ QCD simulations in [24] showing the expected large effects due to the sea quarks. It is also interesting to compare $c(r)$ measured on the lattice to the expectations from phenomenological potentials like the Cornell Eq. (2.5) or the Richardson Eq. (2.6) potential. In particular the Cornell potential yields a constant $c(r) \equiv -0.52$.

Figure 16 shows our data for $c(\tilde{r})$ as a function of $\tilde{r}/r_0$ computed on the ensemble E250 at the physical point. Notice that string breaking happens at $\tilde{r}/r_0 \approx 2.6$ [12] so the data shown are for distances well below this threshold. For $\tilde{r} \to 0$ we plot the perturbative curve (black) obtained using the 4-loop β-function for the coupling α_c as given in Appendix B.1 of [24] using for the Λ parameter the value in Eq. (6.10). The grey band represents the uncertainty in the Λ parameter from Eq. (6.10). We see that our data do not reach distances small enough to make contact with the perturbative behaviour. In the region 0.5–1.3 r_0 the data points follows remarkably close the curve of the Richardson potential (blue) using Eq. (6.10) for the Λ parameter. The blue band represents the uncertainty of the Λ parameter from Eq. (6.10). We observe a dependence of c on the distance which is clearly different from the constant behaviour assumed in the Cornell model. The statistical quality of the data degrades fast with increasing distance. Together with the noise-to-signal problem of the Wilson loops there is a factor r^3 in the definition of c which amplifies further the problem at large distances r. The situation can be improved if multi-level sampling algorithms with dynamical fermions [107] are applied but this is beyond the scope of the present study.

Acknowledgements We thank Rainer Sommer for valuable discussions. The authors gratefully acknowledge the Gauss Centre for Supercomputing e.V. (www.gauss-centre.eu) for funding this project by providing computing time on the GCS Supercomputer SuperMUC-NG at Leibniz Supercomputing Centre (http://www.lrz.de). Some computations were carried out on the PLEIADES cluster at the University of Wuppertal, which was supported by the Deutsche Forschungsgemeinschaft (DFG) and the Bundesministerium für Bildung und Forschung (BMBF). The work is supported by the German Research Foundation (DFG) research unit FOR5269 "Future methods for studying confined gluons in QCD". The project is receiving funding from the programme "Netzwerke 2021", an initiative of the Ministry of Culture and Science of the State of Northrhine Westphalia, in the NRW-FAIR network, funding code NW21-024-A (R.H.). The sole responsibility for the content of this publication lies with the authors.

Funding DFG under FOR5269, Ministry of Culture and Science of the State of Northrhine Westphalia with funding code NW21-024-A.

Data Availability Statement Data will be made available on reasonable request. [Author's comment: The datasets generated during and/or analysed during the current study are available from the corresponding author on reasonable request.]

Code Availability Statement Code/software will be made available on reasonable request. [Author's comment: The code/software generated during and/or analysed during the current study is available from the corresponding author on reasonable request.

Funded by SCOAP[3].

Appendix

A.1 Wilson-loop parameters

See Table 3.

Table 3 Maximal temporal and spatial sizes of the Wilson loops, smearing levels and number of measurements are listed for each ensemble

β	id	$T_{\max}/a$	$r_{\max}/a$	Smearing	N_{meas}
3.40	H101	24	16	8, 14	2016
	H102-0	24	16	8, 14	997
	H102-1	24	16	8, 14	1008
	H105	24	16	8, 14	1970
	C101	24	16	8, 14	2000
3.46	B450	24	16	11, 18	1612
	S400	24	16	11, 18	2873
	D450	24	16	11, 18	500
	D452	24	16	11, 18	999
3.55	N202	24	16	15, 25	1902
	N203	24	16	15, 25	1543
	N200	24	16	15, 25	1712
	D200	24	16	15, 25	2001
	E250	24	16	15, 25	950
3.70	N300-0	28	20	20, 30	507
	N300-1	28	20	20, 30	1479
	J303	28	20	20, 30	1073
	E300	28	20	20, 30, 45, 60	1137
3.85	J500	32	24	25, 35	1444
	J501	32	24	25, 35	3559

Table 4 Values of r_I/a used for V' and $\tilde{r}/a$ for V'' for one level of HYP2 smearing in static quark action

r/a	r_I/a	$\tilde{r}/a$
4	3.568	4.053
5	4.541	5.030
6	5.523	6.015
7	6.510	7.001
8	7.504	7.992
9	8.499	8.987
10	9.497	9.984
11	10.496	10.983
12	11.495	11.982
13	12.495	12.982
14	13.494	13.983
15	14.494	14.983
16	15.494	15.984
17	16.495	16.984
18	17.495	17.985
19	18.495	18.985
20	19.495	19.986

A.2 Improved distance

To determine the improved distance we calculate the momentum integral Eq. (4.6) numerically as a $L/a \to \infty$ limit of discrete momentum sums. The sums, which we denote by $G(L/a)$ were computed for lattices of sizes $L/a = 64$ up to $L/a = 512$. To extrapolate to an infinite lattice we use the ansatz $G(L/a) = G(\infty) + c_2(a/L)^3 + c_3(a/L)^5$, see appendix A of [24]. Other ansätze including the terms $c_4(a/L)^7$ and $c_5(a/L)^9$ were tried as well to estimate the systematics. Using Eq. (4.5) we find r_I. The improved distance for $\tilde{r}/a$ is determined similarly (Table 4).

A.3 Raw results per ensemble

See Table 5.

A.4 Fit results

See Table 6.

Table 5 The values of r_0/a, r_1/a, and the ratio r_0/r_1 for all ensembles

β	id	r_0/a	r_1/a	r_0/r_1
3.40	H101	5.81(7)	3.842(13)	1.511(19)
	H102	5.87(8)	3.886(14)	1.511(20)
	H105	5.89(8)	3.860(11)	1.526(21)
	C101	5.94(4)	3.874(8)	1.534(10)
3.46	B450	6.57(8)	4.299(19)	1.527(20)
	S400	6.71(7)	4.331(17)	1.549(15)
	D450	6.62(3)	4.327(9)	1.530(9)
	D452	6.69(3)	4.340(8)	1.542(8)
3.55	N202	7.72(6)	5.066(19)	1.525(14)
	N203	7.77(5)	5.036(14)	1.543(10)
	N200	7.78(6)	5.025(13)	1.549(12)
	D200	7.69(3)	5.041(9)	1.526(6)
	E250	7.79(2)	5.054(5)	1.541(5)
3.70	N300	9.77(11)	6.413(31)	1.525(20)
	J303	9.84(5)	6.432(13)	1.530(8)
	E300	9.84(11)	6.529(24)	1.506(18)
3.85	J500	12.43(9)	8.163(28)	1.523(12)
	J501	12.61(15)	8.226(32)	1.533(19)

Table 6 The different fits together with the cuts used to find the scales r_0, r_1, and the ratio r_0/r_1 at physical point used in Figs. 10 and 11

Fit #	Cut method	r_0 [fm]	χ^2/d.o.f	r_1 [fm]	χ^2/d.o.f	r_0/r_1	χ^2/d.o.f
Fit 1	No cuts	0.4758(57)	12.6/15	0.3100(32)	30.4/15	1.5344(95)	13.6/15
	$m_\pi < 400$ MeV	0.4750(57)	10.5/10	0.3100(32)	27.5/10	1.5325(94)	12.0/10
	$\beta > 3.4$	0.4724(61)	9.7/11	0.3104(33)	27.0/11	1.5224(127)	10.0/11
	$\beta > 3.46$	0.4728(73)	7.2/7	0.3130(35)	18.4/7	1.5142(199)	7.6/7
	$m_\pi < 400$ MeV and $\beta > 3.4$	0.4716(62)	8.1/7	0.3104(33)	25.0/7	1.5198(123)	8.5/7
Fit 2	No cuts	0.4763(57)	11.1/14	0.3099(32)	30.1/14	1.5341(93)	13.1/14
	$m_\pi < 400$ MeV	0.4778(59)	4.2/9	0.3102(33)	23.6/9	1.5396(95)	8.1/9
	$\beta > 3.4$	0.4730(62)	8.6/10	0.3104(33)	26.3/10	1.5222(125)	9.8/10
	$\beta > 3.46$	0.4731(73)	6.5/6	0.3127(35)	18.2/6	1.5124(186)	7.2/6
	$m_\pi < 400$ MeV and $\beta > 3.4$	0.4745(64)	2.3/6	0.3107(33)	21.0/6	1.5272(126)	5.5/6
Fit 3	No cuts	0.4762(63)	12.4/14	0.3099(33)	30.7/14	1.5350(105)	13.4/14
	$m_\pi < 400$ MeV	0.4755(68)	10.4/9	0.3099(33)	27.7/9	1.5351(149)	11.5/9
	$\beta > 3.4$	0.4724(78)	9.8/10	0.3104(35)	27.2/10	1.5225(152)	10.0/10
	$\beta > 3.46$	0.4724(175)	7.2/6	0.3144(49)	16.4/6	1.5114(295)	7.5/6
	$m_\pi < 400$ MeV and $\beta > 3.4$	0.4716(86)	8.1/6	0.3103(36)	25.0/6	1.5213(230)	8.5/6
Fit 4	No cuts	0.4769(61)	12.3/14	0.3106(33)	30.0/14	1.5351(109)	13.0/14
	$m_\pi < 400$ MeV	0.4762(66)	10.3/9	0.3106(33)	27.1/9	1.5350(141)	11.4/14
	$\beta > 3.4$	0.4733(73)	9.66/10	0.3108(35)	26.8/10	1.5231(160)	10.0/14
	$\beta > 3.46$	0.4729(166)	7.1/6	0.3145(48)	16.4/6	1.5121(334)	8.1/14
	$m_\pi < 400$ MeV and $\beta > 3.4$	0.4726(82)	8.0/6	0.3107(36)	24.6/6	1.5220(216)	8.3/14

References

1. R. Sommer, A new way to set the energy scale in lattice gauge theories and its applications to the static force and alpha-s in SU(2) Yang–Mills theory. Nucl. Phys. B **411**, 839–854 (1994). https://doi.org/10.1016/0550-3213(94)90473-1. arXiv:hep-lat/9310022
2. K.G. Wilson, Confinement of quarks. Phys. Rev. D **10**, 2445–2459 (1974). https://doi.org/10.1103/PhysRevD.10.2445
3. A. Di Giacomo, M. Maggiore, S. Olejnik, Evidence for flux tubes from cooled QCD configurations. Phys. Lett. B **236**, 199–202 (1990). https://doi.org/10.1016/0370-2693(90)90828-T
4. A. Di Giacomo, M. Maggiore, S. Olejnik, Confinement and chromoelectric flux tubes in lattice QCD. Nucl. Phys. B **347**, 441–460 (1990). https://doi.org/10.1016/0550-3213(90)90567-W
5. V. Singh, D.A. Browne, R.W. Haymaker, Structure of Abrikosov vortices in SU(2) lattice gauge theory. Phys. Lett. B **306**, 115–119 (1993). https://doi.org/10.1016/0370-2693(93)91146-E. arXiv:hep-lat/9301004
6. G.S. Bali, K. Schilling, C. Schlichter, Observing long color flux tubes in SU(2) lattice gauge theory. Phys. Rev. D **51**, 5165–5198 (1995). https://doi.org/10.1103/PhysRevD.51.5165. arXiv:hep-lat/9409005
7. G.S. Bali, QCD forces and heavy quark bound states. Phys. Rep. **343**, 1–136 (2001). https://doi.org/10.1016/S0370-1573(00)00079-X. arXiv:hep-ph/0001312
8. M. Lüscher, P. Weisz, Quark confinement and the bosonic string. JHEP **07**, 049 (2002). https://doi.org/10.1088/1126-6708/2002/07/049. arXiv:hep-lat/0207003
9. J. Greensite, S. Olejnik, M. Polikarpov, S. Syritsyn, V. Zakharov, Localized eigenmodes of covariant Laplacians in the Yang–Mills vacuum. Phys. Rev. D **71**, 114507 (2005). https://doi.org/10.1103/PhysRevD.71.114507. arXiv:hep-lat/0504008
10. O. Andreev, String breaking, baryons, medium, and gauge/string duality. Phys. Rev. D **101**(10), 106003 (2020). https://doi.org/10.1103/PhysRevD.101.106003. arXiv:2003.09880 [hep-ph]
11. J. Bulava, B. Hörz, F. Knechtli, V. Koch, G. Moir, C. Morningstar, M. Peardon, String breaking by light and strange quarks in QCD. Phys. Lett. B **793**, 493–498 (2019). https://doi.org/10.1016/j.physletb.2019.05.018. arXiv:1902.04006 [hep-lat]
12. J. Bulava, F. Knechtli, V. Koch, C. Morningstar, M. Peardon, The quark-mass dependence of the potential energy between static colour sources in the QCD vacuum with light and strange quarks. Phys. Lett. B **854**, 138754 (2024). https://doi.org/10.1016/j.physletb.2024.138754. arXiv:2403.00754 [hep-lat]
13. C.W. Bernard, T. Burch, K. Orginos, D. Toussaint, T.A. DeGrand, C.E. DeTar, S.A. Gottlieb, U.M. Heller, J.E. Hetrick, B. Sugar, The Static quark potential in three flavor QCD. Phys. Rev. D **62**, 034503 (2000). https://doi.org/10.1103/PhysRevD.62.034503. arXiv:hep-lat/0002028
14. A. Bazavov, P. Petreczky, J.H. Weber, Equation of state in 2+1 flavor QCD at high temperatures. Phys. Rev. D **97**(1), 014510 (2018). https://doi.org/10.1103/PhysRevD.97.014510. arXiv:1710.05024 [hep-lat]
15. M. Bruno et al., Simulation of QCD with $N_f = 2 + 1$ flavors of non-perturbatively improved Wilson fermions. JHEP **02**, 043 (2015). https://doi.org/10.1007/JHEP02(2015)043. arXiv:1411.3982 [hep-lat]
16. D. Mohler, S. Schaefer, J. Simeth, CLS 2+1 flavor simulations at physical light- and strange-quark masses. EPJ Web Conf. **175**, 02010 (2018). https://doi.org/10.1051/epjconf/201817502010. arXiv:1712.04884 [hep-lat]
17. M. Lüscher, Properties and uses of the Wilson flow in lattice QCD. JHEP **08**, 071 (2010). https://doi.org/10.1007/JHEP08(2010)071. arXiv:1006.4518 [hep-lat]. [Erratum: JHEP **03**, 092 (2014)]
18. M. Peter, The static potential in QCD: a full two loop calculation. Nucl. Phys. B **501**, 471–494 (1997). https://doi.org/10.1016/S0550-3213(97)00373-8. arXiv:hep-ph/9702245
19. Y. Schröder, The static potential in QCD to two loops. Phys. Lett. B **447**, 321–326 (1999). https://doi.org/10.1016/S0370-2693(99)00010-6. arXiv:hep-ph/9812205
20. M. Melles, The static QCD potential in coordinate space with quark masses through two loops. Phys. Rev. D **62**, 074019 (2000). https://doi.org/10.1103/PhysRevD.62.074019. arXiv:hep-ph/0001295
21. C. Anzai, Y. Kiyo, Y. Sumino, Static QCD potential at three-loop order. Phys. Rev. Lett. **104**, 112003 (2010). https://doi.org/10.1103/PhysRevLett.104.112003. arXiv:0911.4335 [hep-ph]
22. N. Brambilla, A. Vairo, X. Garcia i Tormo, J. Soto, The QCD static energy at NNNLL. Phys. Rev. D **80**, 034016 (2009). https://doi.org/10.1103/PhysRevD.80.034016. arXiv:0906.1390 [hep-ph]
23. S.J. Brodsky, M. Melles, J. Rathsman, The two loop scale dependence of the static QCD potential including quark masses. Phys. Rev. D **60**, 096006 (1999). https://doi.org/10.1103/PhysRevD.60.096006. arXiv:hep-ph/9906324
24. M. Donnellan, F. Knechtli, B. Leder, R. Sommer, Determination of the static potential with dynamical fermions. Nucl. Phys. B **849**, 45–63 (2011). https://doi.org/10.1016/j.nuclphysb.2011.03.013. arXiv:1012.3037 [hep-lat]
25. T. van Ritbergen, J.A.M. Vermaseren, S.A. Larin, The four loop beta function in quantum chromodynamics. Phys. Lett. B **400**, 379–384 (1997). https://doi.org/10.1016/S0370-2693(97)00370-5. arXiv:hep-ph/9701390
26. M. Czakon, The four-loop QCD beta-function and anomalous dimensions. Nucl. Phys. B **710**, 485–498 (2005). https://doi.org/10.1016/j.nuclphysb.2005.01.012. arXiv:hep-ph/0411261
27. Y. Nambu, QCD and the string model. Phys. Lett. B **80**, 372–376 (1979). https://doi.org/10.1016/0370-2693(79)91193-6
28. E. Eichten, K. Gottfried, T. Kinoshita, K.D. Lane, T.-M. Yan, Charmonium: the model. Phys. Rev. D **17**, 3090 (1978). https://doi.org/10.1103/PhysRevD.17.3090. [Erratum: Phys. Rev. D **21**, 313 (1980)]
29. E. Eichten, K. Gottfried, T. Kinoshita, K.D. Lane, T.-M. Yan, Charmonium: comparison with experiment. Phys. Rev. D **21**, 203 (1980). https://doi.org/10.1103/PhysRevD.21.203
30. J.L. Richardson, The heavy quark potential and the upsilon, J/psi systems. Phys. Lett. B **82**, 272–274 (1979). https://doi.org/10.1016/0370-2693(79)90753-6
31. SESAM Collaboration, G.S. Bali, H. Neff, T. Duessel, T. Lippert, K. Schilling, Observation of string breaking in QCD. Phys. Rev. D **71**, 114513 (2005). https://doi.org/10.1103/PhysRevD.71.114513. arXiv:hep-lat/0505012
32. M. Della Morte, A. Shindler, R. Sommer, On lattice actions for static quarks. JHEP **08**, 051 (2005). https://doi.org/10.1088/1126-6708/2005/08/051. arXiv:hep-lat/0506008
33. A. Grimbach, D. Guazzini, F. Knechtli, F. Palombi, O(a) improvement of the HYP static axial and vector currents at one-loop order of perturbation theory. JHEP **03**, 039 (2008). https://doi.org/10.1088/1126-6708/2008/03/039. arXiv:0802.0862 [hep-lat]
34. Flavour Lattice Averaging Group (FLAG) Collaboration, Y. Aoki et al., FLAG review 2021. Eur. Phys. J. C **82**(10), 869 (2022). https://doi.org/10.1140/epjc/s10052-022-10536-1. arXiv:2111.09849 [hep-lat]
35. BMW Collaboration, S. Borsányi, S. Dürr, Z. Fodor, C. Hoelbling, S.D. Katz, S. Krieg, T. Kurth, L. Lellouch, T. Lippert, C. McNeile, High-precision scale setting in lattice QCD. JHEP **09**, 010 (2012). https://doi.org/10.1007/JHEP09(2012)010. arXiv:1203.4469 [hep-lat]
36. M. Lüscher, P. Weisz, On-shell improved lattice gauge theories. Commun. Math. Phys. **98**(3), 433 (1985). https://doi.org/10.1007/BF01205792. [Erratum: Commun. Math. Phys. **98**, 433 (1985)]

37. B. Sheikholeslami, R. Wohlert, Improved continuum limit lattice action for QCD with Wilson fermions. Nucl. Phys. B **259**, 572 (1985). https://doi.org/10.1016/0550-3213(85)90002-1
38. J. Bulava, S. Schaefer, Improvement of $N_f = 3$ lattice QCD with Wilson fermions and tree-level improved gauge action. Nucl. Phys. B **874**, 188–197 (2013). https://doi.org/10.1016/j.nuclphysb.2013.05.019. arXiv:1304.7093 [hep-lat]
39. M. Lüscher, S. Schaefer, Lattice QCD without topology barriers. JHEP **07**, 036 (2011). https://doi.org/10.1007/JHEP07(2011)036. arXiv:1105.4749 [hep-lat]
40. S. Duane, A.D. Kennedy, B.J. Pendleton, D. Roweth, Hybrid Monte Carlo. Phys. Lett. B **195**, 216–222 (1987). https://doi.org/10.1016/0370-2693(87)91197-X
41. M. Hasenbusch, Speeding up the hybrid Monte Carlo algorithm for dynamical fermions. Phys. Lett. B **519**, 177–182 (2001). https://doi.org/10.1016/S0370-2693(01)01102-9. arXiv:hep-lat/0107019
42. A.D. Kennedy, I. Horvath, S. Sint, A new exact method for dynamical fermion computations with nonlocal actions. Nucl. Phys. B Proc. Suppl. **73**, 834–836 (1999). https://doi.org/10.1016/S0920-5632(99)85217-7. arXiv:hep-lat/9809092
43. M. Lüscher, S. Schaefer, Lattice QCD with open boundary conditions and twisted-mass reweighting. Comput. Phys. Commun. **184**, 519–528 (2013). https://doi.org/10.1016/j.cpc.2012.10.003. arXiv:1206.2809 [hep-lat]
44. M. Lüscher. https://luscher.web.cern.ch/luscher/openQCD/
45. M. Lüscher, F. Palombi, Fluctuations and reweighting of the quark determinant on large lattices. PoS **LATTICE2008**, 049 (2008). https://doi.org/10.22323/1.066.0049. arXiv:0810.0946 [hep-lat]
46. S. Kuberski, Low-mode deflation for twisted-mass and RHMC reweighting in lattice QCD. Comput. Phys. Commun. **300**, 109173 (2024). https://doi.org/10.1016/j.cpc.2024.109173. arXiv:2306.02385 [hep-lat]
47. D. Mohler, S. Schaefer, Remarks on strange-quark simulations with Wilson fermions. Phys. Rev. D **102**(7), 074506 (2020). https://doi.org/10.1103/PhysRevD.102.074506. arXiv:2003.13359 [hep-lat]
48. B. Straßberger et al., Scale setting for CLS 2+1 simulations. PoS **LATTICE2021**, 135 (2022). https://doi.org/10.22323/1.396.0135. arXiv:2112.06696 [hep-lat]
49. M. Bruno, T. Korzec, S. Schaefer, Setting the scale for the CLS 2+1 flavor ensembles. Phys. Rev. D **95**(7), 074504 (2017). https://doi.org/10.1103/PhysRevD.95.074504. arXiv:1608.08900 [hep-lat]
50. ALPHA Collaboration, U. Wolff, Monte Carlo errors with less errors. Comput. Phys. Commun. **156**, 143–153 (2004). https://doi.org/10.1016/S0010-4655(03)00467-3. arXiv:hep-lat/0306017. [Erratum: Comput. Phys. Commun. **176**, 383 (2007)]
51. ALPHA Collaboration, S. Schaefer, R. Sommer, F. Virotta, Critical slowing down and error analysis in lattice QCD simulations. Nucl. Phys. B **845**, 93–119 (2011). https://doi.org/10.1016/j.nuclphysb.2010.11.020. arXiv:1009.5228 [hep-lat]
52. H. Simma, R. Sommer, F. Virotta, General error computation in lattice gauge theory. Internal notes of the ALPHA collaboration (2012–2014)
53. A. Ramos, Automatic differentiation for error analysis of Monte Carlo data. Comput. Phys. Commun. **238**, 19–35 (2019). https://doi.org/10.1016/j.cpc.2018.12.020. arXiv:1809.01289 [hep-lat]
54. F. Joswig, S. Kuberski, J.T. Kuhlmann, J. Neuendorf, pyerrors: A python framework for error analysis of Monte Carlo data. Comput. Phys. Commun. **288**, 108750 (2023). https://doi.org/10.1016/j.cpc.2023.108750. arXiv:2209.14371 [hep-lat]
55. B. Leder, Wilson loop computation (2015). https://github.com/bjoern-leder/wloop
56. A. Hasenfratz, F. Knechtli, Flavor symmetry and the static potential with hypercubic blocking. Phys. Rev. D **64**, 034504 (2001). https://doi.org/10.1103/PhysRevD.64.034504. arXiv:hep-lat/0103029
57. E. Eichten, B.R. Hill, An effective field theory for the calculation of matrix elements involving heavy quarks. Phys. Lett. B **234**, 511–516 (1990). https://doi.org/10.1016/0370-2693(90)92049-O
58. N.A. Campbell, A. Huntley, C. Michael, Heavy quark potentials and hybrid mesons from SU(3) lattice gauge theory. Nucl. Phys. B **306**, 51–62 (1988). https://doi.org/10.1016/0550-3213(88)90170-8
59. ALPHA Collaboration, M. Guagnelli, R. Sommer, H. Wittig, Precision computation of a low-energy reference scale in quenched lattice QCD. Nucl. Phys. B **535**, 389–402 (1998). https://doi.org/10.1016/S0550-3213(98)00599-9. arXiv:hep-lat/9806005
60. M. Lüscher, U. Wolff, How to calculate the elastic scattering matrix in two-dimensional quantum field theories by numerical simulation. Nucl. Phys. B **339**, 222–252 (1990). https://doi.org/10.1016/0550-3213(90)90540-T
61. B. Blossier, M. Della Morte, G. von Hippel, T. Mendes, R. Sommer, On the generalized eigenvalue method for energies and matrix elements in lattice field theory. JHEP **04**, 094 (2009). https://doi.org/10.1088/1126-6708/2009/04/094. arXiv:0902.1265 [hep-lat]
62. M. Fischer, B. Kostrzewa, J. Ostmeyer, K. Ottnad, M. Ueding, C. Urbach, On the generalised eigenvalue method and its relation to Prony and generalised pencil of function methods. Eur. Phys. J. A **56**(8), 206 (2020). https://doi.org/10.1140/epja/s10050-020-00205-w
63. G. Parisi, R. Petronzio, F. Rapuano, A measurement of the string tension near the continuum limit. Phys. Lett. B **128**, 418–420 (1983). https://doi.org/10.1016/0370-2693(83)90930-9
64. M. Lüscher, P. Weisz, Locality and exponential error reduction in numerical lattice gauge theory. JHEP **09**, 010 (2001). https://doi.org/10.1088/1126-6708/2001/09/010. arXiv:hep-lat/0108014
65. C. Alexandrou, P. De Forcrand, A. Tsapalis, The static three quark SU(3) and four quark SU(4) potentials. Phys. Rev. D **65**, 054503 (2002). https://doi.org/10.1103/PhysRevD.65.054503. arXiv:hep-lat/0107006
66. A. Hasenfratz, R. Hoffmann, F. Knechtli, The static potential with hypercubic blocking. Nucl. Phys. B Proc. Suppl. **106**, 418–420 (2002). https://doi.org/10.1016/S0920-5632(01)01733-9. arXiv:hep-lat/0110168
67. R. Hoffmann, The static potential with hypercubic blocking. Diploma thesis (2002)
68. T.M.B. Asmussen, R. Höllwieser, F. Knechtli, T. Korzec, The determination of r_0 and r_1 in Nf=2+1 QCD. PoS **LATTICE2023**, 296 (2024). https://doi.org/10.22323/1.453.0296. arXiv:2312.14726 [hep-lat]
69. C. Aubin, K. Orginos, D. Armstrong, V. Burkert, J.-P. Chen, W. Detmold, J. Dudek, W. Melnitchouk, D. Richards, A new approach for delta form factors, in *AIP Conference Proceedings* (AIP, 2011), pp. 621–624. https://doi.org/10.1063/1.3647217
70. C. Aubin, K. Orginos, An improved method for extracting matrix elements from lattice three-point functions. PoS **Lattice 2011**, 148 (2012). https://doi.org/10.22323/1.139.0148
71. R.W. Schiel, Expanding the interpolator basis in the variational method to explicitly account for backward running states. Phys. Rev. D **92**, 034512 (2015). https://doi.org/10.1103/PhysRevD.92.034512
72. K. Ottnad, T. Harris, H. Meyer, G. von Hippel, J. Wilhelm, H. Wittig, Nucleon average quark momentum fraction with nf = 2+1 Wilson fermions. EPJ Web Conf. **175**, 06026 (2018). https://doi.org/10.1051/epjconf/201817506026
73. F. Niedermayer, P. Rufenacht, U. Wenger, Fixed point gauge actions with fat links: scaling and glueballs. Nucl.

Phys. B **597**, 413–450 (2001). https://doi.org/10.1016/S0550-3213(00)00731-8. arXiv:hep-lat/0007007
74. H. Akaike, A new look at the statistical model identification. IEEE Trans Autom Control **19**(6), 716–723 (1974). https://doi.org/10.1109/TAC.1974.1100705
75. W.I. Jay, E.T. Neil, Bayesian model averaging for analysis of lattice field theory results. Phys. Rev. D **103**, 114502 (2021). https://doi.org/10.1103/PhysRevD.103.114502. arXiv:2008.01069 [stat.ME]
76. E.T. Neil, J.W. Sitison, Improved information criteria for Bayesian model averaging in lattice field theory. Phys. Rev. D **109**(1), 014510 (2024). https://doi.org/10.1103/PhysRevD.109.014510. arXiv:2208.14983 [stat.ME]
77. ALPHA Collaboration, I. Campos Plasencia, M. Dalla Brida, G.M. de Divitiis, A. Lytle, M. Papinutto, L. Pirelli, A. Vladikas, Nonperturbative running of the tensor operator for Nf = 3 QCD from the chirally rotated Schrödinger functional. Phys. Rev. D **109**(5), 054511 (2024). https://doi.org/10.1103/PhysRevD.109.054511. arXiv:2311.15046 [hep-lat]
78. K. Symanzik, Cutoff dependence in lattice ϕ_4^4 theory. NATO Sci. Ser. B **59**, 313–330 (1980). https://doi.org/10.1007/978-1-4684-7571-5_18
79. J. Balog, F. Niedermayer, P. Weisz, Logarithmic corrections to O(a**2) lattice artifacts. Phys. Lett. B **676**, 188–192 (2009). https://doi.org/10.1016/j.physletb.2009.04.082. arXiv:0901.4033 [hep-lat]
80. N. Husung, P. Marquard, R. Sommer, Asymptotic behavior of cutoff effects in Yang–Mills theory and in Wilson's lattice QCD. Eur. Phys. J. C **80**(3), 200 (2020). https://doi.org/10.1140/epjc/s10052-020-7685-4. arXiv:1912.08498 [hep-lat]
81. N. Husung, P. Marquard, R. Sommer, The asymptotic approach to the continuum of lattice QCD spectral observables. Phys. Lett. B **829**, 137069 (2022). https://doi.org/10.1016/j.physletb.2022.137069. arXiv:2111.02347 [hep-lat]
82. European Twisted Mass Collaboration, N. Carrasco et al., Up, down, strange and charm quark masses with $N_f = 2+1+1$ twisted mass lattice QCD. Nucl. Phys. B **887**, 19–68 (2014). https://doi.org/10.1016/j.nuclphysb.2014.07.025. arXiv:1403.4504 [hep-lat]
83. MILC Collaboration, A. Bazavov et al., MILC results for light pseudoscalars. PoS **CD09**, 007 (2009). https://doi.org/10.22323/1.086.0007. arXiv:0910.2966 [hep-ph]
84. Y.-B. Yang et al., Charm and strange quark masses and f_{D_s} from overlap fermions. Phys. Rev. D **92**(3), 034517 (2015). https://doi.org/10.1103/PhysRevD.92.034517. arXiv:1410.3343 [hep-lat]
85. R.J. Dowdall, C.T.H. Davies, G.P. Lepage, C. McNeile, V_{us} from pi and K decay constants in full lattice QCD with physical u, d, s and c quarks. Phys. Rev. D **88**, 074504 (2013). https://doi.org/10.1103/PhysRevD.88.074504. arXiv:1303.1670 [hep-lat]
86. MILC Collaboration, A. Bazavov et al., Results for light pseudoscalar mesons. PoS **LATTICE2010**, 074 (2010). https://doi.org/10.22323/1.105.0074. arXiv:1012.0868 [hep-lat]
87. HotQCD Collaboration, A. Bazavov et al., Equation of state in (2+1)-flavor QCD. Phys. Rev. D **90**, 094503 (2014). https://doi.org/10.1103/PhysRevD.90.094503. arXiv:1407.6387 [hep-lat]
88. RBC, UKQCD Collaboration, Y. Aoki et al., Continuum limit physics from 2+1 flavor domain wall QCD. Phys. Rev. D **83**, 074508 (2011). https://doi.org/10.1103/PhysRevD.83.074508. arXiv:1011.0892 [hep-lat]
89. A. Gray, I. Allison, C.T.H. Davies, E. Dalgic, G.P. Lepage, J. Shigemitsu, M. Wingate, The Upsilon spectrum and m(b) from full lattice QCD. Phys. Rev. D **72**, 094507 (2005). https://doi.org/10.1103/PhysRevD.72.094507. arXiv:hep-lat/0507013
90. C. Aubin, C. Bernard, C. DeTar, J. Osborn, S. Gottlieb, E.B. Gregory, D. Toussaint, U.M. Heller, J.E. Hetrick, R. Sugar, Light hadrons with improved staggered quarks: approaching the continuum limit. Phys. Rev. D **70**, 094505 (2004). https://doi.org/10.1103/PhysRevD.70.094505. arXiv:hep-lat/0402030
91. HPQCD Collaboration, C.T.H. Davies, E. Follana, I.D. Kendall, G.P. Lepage, C. McNeile, Precise determination of the lattice spacing in full lattice QCD. Phys. Rev. D **81**, 034506 (2010). https://doi.org/10.1103/PhysRevD.81.034506. arXiv:0910.1229 [hep-lat]
92. MILC Collaboration, A. Bazavov et al., Nonperturbative QCD simulations with 2+1 flavors of improved staggered quarks. Rev. Mod. Phys. **82**, 1349–1417 (2010). https://doi.org/10.1103/RevModPhys.82.1349. arXiv:0903.3598 [hep-lat]
93. PACS-CS Collaboration, S. Aoki et al., 2+1 Flavor lattice QCD toward the physical point. Phys. Rev. D **79**, 034503 (2009). https://doi.org/10.1103/PhysRevD.79.034503. arXiv:0807.1661 [hep-lat]
94. HPQCD Collaboration, R.J. Dowdall et al., The Upsilon spectrum and the determination of the lattice spacing from lattice QCD including charm quarks in the sea. Phys. Rev. D **85**, 054509 (2012). https://doi.org/10.1103/PhysRevD.85.054509. arXiv:1110.6887 [hep-lat]
95. A. Bazavov et al., The chiral and deconfinement aspects of the QCD transition. Phys. Rev. D **85**, 054503 (2012). https://doi.org/10.1103/PhysRevD.85.054503. arXiv:1111.1710 [hep-lat]
96. TUMQCD Collaboration, N. Brambilla, R.L. Delgado, A.S. Kronfeld, V. Leino, P. Petreczky, S. Steinbeißer, A. Vairo, J.H. Weber, Static energy in $(2+1+1)$-flavor lattice QCD: scale setting and charm effects. Phys. Rev. D **107**(7), 074503 (2023). https://doi.org/10.1103/PhysRevD.107.074503. arXiv:2206.03156 [hep-lat]
97. ALPHA Collaboration, M. Bruno, J. Finkenrath, F. Knechtli, B. Leder, R. Sommer, Effects of heavy sea quarks at low energies. Phys. Rev. Lett. **114**(10), 102001 (2015). https://doi.org/10.1103/PhysRevLett.114.102001. arXiv:1410.8374 [hep-lat]
98. ALPHA Collaboration, F. Knechtli, T. Korzec, B. Leder, G. Moir, Power corrections from decoupling of the charm quark. Phys. Lett. B **774**, 649–655 (2017). https://doi.org/10.1016/j.physletb.2017.10.025. arXiv:1706.04982 [hep-lat]
99. M. Dalla Brida, Past, present, and future of precision determinations of the QCD parameters from lattice QCD. Eur. Phys. J. A **57**(2), 66 (2021). https://doi.org/10.1140/epja/s10050-021-00381-3. arXiv:2012.01232
100. ALPHA Collaboration, M. Bruno, M. Dalla Brida, P. Fritzsch, T. Korzec, A. Ramos, S. Schaefer, H. Simma, S. Sint, R. Sommer, QCD coupling from a nonperturbative determination of the three-flavor Λ parameter. Phys. Rev. Lett. **119**(10), 102001 (2017). https://doi.org/10.1103/PhysRevLett.119.102001. arXiv:1706.03821 [hep-lat]
101. TUMQCD Collaboration, A. Bazavov, N. Brambilla, X. Garcia i Tormo, P. Petreczky, J. Soto, A. Vairo, J.H. Weber, Determination of the QCD coupling from the static energy and the free energy. Phys. Rev. D **100**(11), 114511 (2019). https://doi.org/10.1103/PhysRevD.100.114511. arXiv:1907.11747 [hep-lat]
102. S. Cali, K. Cichy, P. Korcyl, J. Simeth, Running coupling constant from position-space current-current correlation functions in three-flavor lattice QCD. Phys. Rev. Lett. **125**, 242002 (2020). https://doi.org/10.1103/PhysRevLett.125.242002. arXiv:2003.05781 [hep-lat]
103. C. Ayala, X. Lobregat, A. Pineda, Determination of $\alpha(M_z)$ from an hyperasymptotic approximation to the energy of a static quark–antiquark pair. JHEP **09**, 016 (2020). https://doi.org/10.1007/JHEP09(2020)016. arXiv:2005.12301 [hep-ph]
104. PACS-CS Collaboration, S. Aoki et al., Precise determination of the strong coupling constant in $N_f = 2+1$ lattice QCD with the Schrodinger functional scheme. JHEP **10**, 053 (2009). https://doi.org/10.1088/1126-6708/2009/10/053. arXiv:0906.3906 [hep-lat]
105. K. Maltman, D. Leinweber, P. Moran, A. Sternbeck, The realistic lattice determination of alpha(s)(M(Z)) revisited. Phys.

Rev. D **78**, 114504 (2008). https://doi.org/10.1103/PhysRevD.78.114504. arXiv:0807.2020 [hep-lat]

106. C. McNeile, C.T.H. Davies, E. Follana, K. Hornbostel, G.P. Lepage, High-precision c and b masses, and QCD coupling from current-current correlators in lattice and continuum QCD. Phys. Rev. D **82**, 034512 (2010). https://doi.org/10.1103/PhysRevD.82.034512. arXiv:1004.4285 [hep-lat]
107. M. Cè, L. Giusti, S. Schaefer, Domain decomposition, multi-level integration and exponential noise reduction in lattice QCD. Phys. Rev. D **93**(9), 094507 (2016). https://doi.org/10.1103/PhysRevD.93.094507. arXiv:1601.04587 [hep-lat]